accepted version - November 17, 2000

Cooling Flows and Quasars: II. Detailed Models of Feedback Modulated Accretion Flows

Luca Ciotti[1,2] and Jeremiah P. Ostriker
Department of Astrophysical Sciences, Peyton Hall, 08544, NJ, USA

ABSTRACT

Most elliptical galaxies contain central black holes (BHs), and most also contain significant amounts of hot gas capable of accreting on to the central BH due to cooling times short compared to the Hubble time. Why therefore do we not see AGNs at the center of *most* elliptical galaxies rather than in only (at most) a few per cent of them? We propose here the simple idea that *feedback* from accretion events heats the ambient gas, retarding subsequent infall, in a follow up of papers by Binney & Tabor (1995, BT95) and Ciotti & Ostriker (1997, CO97). Even small amounts of accretion on a central BH can cause the release of enough energy to reverse the central inflow, when the Compton temperature ($T_{\rm X}$) of the emitted radiation is higher than the mean galactic gas temperature, the basic assumption of this paper. Well observed nearby AGN (3C 273, 3C 279), having $T_{\rm X}$ near 5×10^8 K, amply satisfy this requirement. In this context, we present a new class of 1D hydrodynamical evolutionary sequences for the gas flows in elliptical galaxies with a massive central BH. The model galaxies are constrained to lie on the Fundamental Plane of elliptical galaxies, and are surrounded by variable amounts of dark matter. Two source terms operate: mass loss from evolving stars, and a secularly declining heating by type Ia supernovae (SNIa). Like the previous models investigated by Ciotti et al. (1991, CDPR) these new models can evolve up to three consecutive evolutionary stages: the wind, outflow, and inflow phases. At this point the presence of the BH alters dramatically the subsequent evolution, because of the energy emitted due to the accreting gas flow. The effect of Compton heating and cooling, of hydrogen and helium photoionization heating, and of bremsstrahlung recycling on the gas flow are investigated by numerical integration of the nonstationary equations of hydrodynamics, in the simplifying assumption of spherical symmetry, and for various values of the accretion efficiency and supernova rates.

The resulting evolution is characterized by strong oscillations, in which very fast and energetic bursts from the BH are followed by longer periods during which the

[1]On leave from Osservatorio Astronomico di Bologna, via Ranzani 1, 40127 Bologna, Italy

[2]Also Scuola Normale Superiore, Piazza dei Cavalieri 7, 56126 Pisa, Italy

X–ray galaxy emission comes from the coronal gas. For a fixed galaxy total mass and structure, the length and the intensity of the bursts depend sensitively on the accretion efficiency and the SNIa rate. For *high efficiency* and *SNIa rate* values, short and strong bursts are followed by a degassing of the galaxy, with a consequent shut–off of the BH followed by a long period when the mass loss from the stellar population replenishes the galaxy, and after which a new cooling catastrophe another accretion event takes place. In this case high accretion rates characterize the BH evolution, but the total mass accreted by the BH is very small. For *low efficiency* and *SNIa rate* values, the luminosity evolution is still characterized by strong intermittencies, but the number of global degassing events is considerably reduced, and for very low efficiency values it completely disappears. The remaining instability is then concentrated in the central galactic regions. We also allow for departures from spherical symmetry by examining scenarios in which the central engine is either an ADAF or a more conventional accretion disk that is optically thick except for a polar region. The general property of highly unstable accretion remains true, with central BHs growing episodically to the mass range $10^8 - 10^9 M_\odot$ (in contrast to $\Delta M_{\rm BH} \gtrsim 10^{10} - 10^{11} M_\odot$, if feedback is ignored). In all cases the duty cycle (fraction of the time that the system will be seen as an AGN) is quite small and in the range $f_{\rm BH} \simeq 10^{-4} - 2 \times 10^{-3}$. Thus, for any reasonable value of the efficiency, the presence of a massive BH at the center of a galaxy seems to be incompatible with the presence of a long–lived cooling flow.

Subject headings: Galaxies: cooling flows – Galaxies: elliptical and lenticular, cD – Galaxies: ISM – X–rays: galaxies – AGN

1. Introduction

As first revealed by *Einstein* observations, normal (non–cD) elliptical galaxies, both isolated or belonging to groups and clusters, can be powerful X–ray sources with 0.5–4.5 keV luminosities $L_{\rm X} \propto L_{\rm B}^{1.8-2.2}$ ranging from $\sim 10^{39}$ to $\sim 10^{42}$ erg s^{-1}, although with a large scatter of more than two orders of magnitude in $L_{\rm X}$ at any fixed optical luminosity $L_{\rm B} \gtrsim 3 \times 10^{10} L_\odot$ (Eskridge, Fabbiano, & Kim 1995). From its spectral properties, this emission is associated with hot gaseous halos around the galaxies, with mean temperatures in the range $0.5 - 1 \times 10^7$ K.

In order to explain this observational finding, the presence of significant amounts of gas is inferred (typical values are in the range $M_{\rm gas} = 10^8$–$10^{11} M_\odot$, see, e.g., Forman et al. 1979, Forman et al. 1985, Canizares et al. 1987, Fabbiano 1989), with computed cooling times often far less than the Hubble time. Consequently, "cooling flow" models have been proposed and extensively investigated (see, e.g., Nulsen, Stewart, & Fabian 1984; Fabian, Nulsen, & Canizares 1984; Sarazin & White 1987, 1988; Vedder, Trester, & Canizares 1988; White & Sarazin 1991; Brighenti & Mathews 1996). While including the essential physics, these models, however, do not provide

a satisfactory account of the X–ray properties of observed elliptical galaxies, as most of them are observed to be much fainter in the X–rays than the models would predict. This is specially true for homogeneous inflow models (see, e.g., Sarazin & White 1988), but serious problems are also encountered by inhomogeneous models. The other main problem of cooling flows is that they do not solve the question of *where* the cool gas is deposited: over a Hubble time an amount of material comparable to the mass of stars in the galactic core flows into the nucleus, while the expected distortions of the central optical surface brightness and velocity dispersion are not observed. Many possible explanations for this problem have been suggested, from local cooling instabilities (see, e.g., Sarazin & Ashe 1989, Bertin & Toniazzo 1995) to star formation biased toward very small masses (Mathews & Brighenti 1999), but no one seems to be easily acceptable. While the cooling included by the cooling flow models is indisputable (it is observed), the question arises as to whether heating sources within the galaxy can equal or exceed (in a time–averaged sense) the gas radiative heat losses.

One possible solution to the previous problems was proposed by CDPR (hereafter "WOI" scenario), who showed with numerical simulations of hot gas flows in elliptical galaxies, that the heating from SNIa could be effective in maintaining low luminosity galaxies in a wind phase over an Hubble time (and so preventing the gas from accumulating in the centre). This scenario does permit one to account both for the correlation and the data dispersion in the $L_{\rm B}$–$L_{\rm X}$ plane. Nevertheless, even in this scenario the most massive galaxies develop an inflow phase, leading to a situation similar to a standard cooling flow, with accretion of significant amounts of gas in their center.

One of the main objections raised against the WOI scenario is the claimed lack of detection of a sufficient amount of iron in the ISM of some ellipticals: the SNIa are good producers of iron, and so one would expect a strong correlation between the evolutionary scenario for galactic gas flows and the amount of iron both in the galactic and in the parent cluster hot gas. For example (following the treatment of Renzini et al. 1993), in the WOI scenario the expected present day iron abundance in galactic flows in units of the solar iron abundance is given by $Z^{\rm Fe}_{\rm flow} \simeq < Z^{\rm Fe}_{\star} > +5\vartheta_{\rm SN}$ (where $\vartheta_{\rm SN} = 1$ corresponds to the standard Tammann's rate (1982) and $< Z^{\rm Fe}_{\star} >$ is the average iron abundance in the stellar component). From an observational point of view Arimoto et al. (1997) quote $< Z^{\rm Fe}_{\star} > \simeq 1$, while according to Mushotzky (1999) $< Z^{\rm Fe}_{\star} > \simeq 0.4$; moreover, Serlemitsos et al. (1993) estimate $Z^{\rm Fe}_{\rm flow} \simeq 0.56$ and 0.20 for NGC 1399 and NGC 4472, respectively. As a consequence the analysis of the available data (under the assumption of solar abundance ratios), suggests an iron abundance in the ISM consistent with no SNIa's enrichment, and even lower than that of the stellar component (see, e.g., Ohashi et al. 1990, Awaki et al. 1991, Ikebe et al. 1992, Serlemitsos et al. 1993, Loewenstein et al. 1994, Mushotzky et al. 1994, Awaki et al. 1994, Arimoto et al. 1997, Matsumoto et al. 1997). This is rather puzzling: in fact, a value of $\vartheta_{\rm SN} = 1/4$ is given by the current optical estimates of the present day SNIa rate (Cappellaro et al. 1997). However, there is an increasing evidence that more complex multi–temperature models with a higher abundance give a better fit to the data (Kim et al. 1996, Buote & Fabian 1998);

for example, the latter authors find a mean value of $Z_{\rm flow}^{\rm Fe} = 0.9 \pm 0.7$, while Buote (1999) derives iron abundances up to twice solar: these figures could be reconciled with $\vartheta_{\rm SN} = 1/4$. Several evolutionary models have been calculated with this rate (Pellegrini & Ciotti 1998, D'Ercole & Ciotti 1998), resulting in the main features of the WOI scenario being preserved, provided the amount of dark matter is properly scaled down. In Sections 2.1 and 4.4 we will return on this point.

From another point of view, there is increasing evidence of the presence of massive BHs at the center of most (if not all) elliptical galaxies (see, e.g., Harms et al. 1994, van der Marel et al. 1997, Richstone 1998, Magorrian et al. 1998). Thus it is natural to ask what can be expected from the interaction of a galactic gas inflow with a massive central BH? In fact, according to the standard interpretation of the AGN phenomenon, a massive BH is at its origin (see, e.g., Rees 1984). We point out here that a strong dependence of the *global* X–ray emission of early type galaxies on the slope of their inner (optical) surface brightness profiles has been found (Pellegrini 1999). Two recent papers considered the effect of the gravitational field of a central BH on the density and temperature profile of cooling flow models (Quataert & Narayan 1999, Brighenti & Mathews 1999). BT95 explored this problem assuming a release of *mechanical* energy in the central regions of the galaxy, due to the interaction between a nuclear jet produced by the accretion and the surrounding ISM, which approach was suggested by the optically thin status of the ISM itself, as computed by the authors with the aid of a simple analytical model. They indicated the circumstances under which the central energy release might impede or reverse the infall.

As will be shown in this paper, the gas over the body of the galaxy is really optically thin, but nevertheless the effect of *energy* exchange between the emitted nuclear *radiation* and the gas flow is dramatic. This effect was studied for accretion on a BH by Ostriker and co–workers (Ostriker et al. 1976, Cowie et al. 1978), and these authors clearly showed how the effect of the Compton heating can be more important than the momentum transfer itself in driving instabilities in the accreting flow. In this context we explore in detail, by numerical integration of the the fully non–stationary equations of hydrodynamics, the modifications on the WOI scenario, assuming the presence at the galaxy center of a massive black hole with initial mass $M_{\rm BH} = 10^8 M_\odot$. A summary of the main features of this new class of models is given in CO97.

An introductory and very simple analysis of this problem can be obtained in a semi–analytical way. For an accretion rate $\dot{M}_{\rm BH}$ on the BH, the emitted luminosity can be easily estimated

$$L_{\rm BH} = 5.67 \times 10^{46} \epsilon \dot{M}_{\rm BH} \quad {\rm erg\ s^{-1}} \tag{1}$$

where $\dot{M}_{\rm BH}$ is in $M_\odot\,{\rm yr}^{-1}$, and ϵ is the accretion efficiency, with $10^{-3} \lesssim \epsilon \lesssim 10^{-1}$ (see equation [9]). It is natural to compare this number with the energy required to *steadily* extract from the galactic potential well the gas lost by the evolving stellar population at a rate $\dot{M}_*$:

$$L_{\rm grav} = 5.67 \times 10^{40} \dot{M}_* \sigma_{\circ *}^2 (U_{**} + U_{*\rm h}\mathcal{R}) \quad {\rm erg\ s^{-1}}. \tag{2}$$

In equation (2) $\dot{M}_*$ is expressed in $M_\odot\,{\rm yr}^{-1}$, the galaxy central velocity dispersion $\sigma_{\circ *}$ is in unit of 300 km s^{-1}, and $\mathcal{R} = M_{\rm h}/M_*$ is the ratio between the dark matter halo mass and the total stellar

mass. The dimensionless functions U_{**} and $U_{*\mathrm{h}}$ depend on the relative density distributions of the galaxy stellar component and of the dark matter halo, and are of the of order of unity.

The ratio between these two luminosities is then given by:

$$\frac{L_{\rm BH}}{L_{\rm grav}} \simeq 6.7\times 10^{16}\frac{\epsilon \dot{M}_{\rm BH}}{(1+\mathcal{R})L_{\rm B}\sigma_{\rm o*}^2 t_{15}^{-1.3}} \simeq \frac{10^6\epsilon}{(1+\mathcal{R})\sigma_{\rm o*}^2}, \tag{3}$$

where t_{15} is the age in 15 Gyr units, and the stellar mass losses have been expressed as function of the present galaxy blue luminosity (in $L_\odot$), $\dot{M}_* \propto L_{\rm B} t_{15}^{-1.3}$ (see Section 2.1 for a detailed description). Numerical simulations shows that a normal elliptical in the inflow phase can accrete at a rate $\sim 1 M_\odot$ yr^{-1} or higher (accretion rates of tens or hundreds solar masses per year are common when inflow are established at early times in giant ellipticals, see, e.g., CDPR). Assuming this value as an estimate for $\dot{M}_{\rm BH}$, it is immediatly realized that the energy emitted by accretion can easily be *orders of magnitude larger* than that formally required to interrupt the cooling flow, even assuming very low efficiency values. Note that this simple energetic argument predicts a greater effect of $L_{\rm BH}$ on the gas flows hosted by small galaxies with respect to those on giant ellipticals; a decrease of the dark matter content goes in the same sense. From the first formula at the r.h.s. of the equation above it is also clear that, at early times, *more* energy is required to extract the gas from the galaxy potential well, but this is compensated by the same fact that more gas is available. If we assume (erroneously) a stationary situation, where the produced $\dot{M}_*$ is accreted on the center, then the second expression in the equation above is obtained, again showing the importance of the radiation emitted in the galactic energy budget.

Obviously, the true situation is by far more complicated. In fact, three main questions arise about the reliability of equation (3). The first concerns how much of $L_{\rm BH}$ is actually *trapped* by the galactic gas and so effectively available for its heating: it is clear indeed that for extremely low opacities, the *effective* energetic balance would be unable to produce a *global degassing*, although strong instabilities may occur. For the moment we will take as a minimal estimate of the absorption that due to the inverse Compton effect, inelastic scattering of the ISM electrons interacting with the high energy photons emitted by the central BH.

We estimate the expected gas opacity using a density profile representative of the inflow models computed in CDPR, $n(r) = n_0/(1+r^2/r_{\rm gas}^2)^{b/2}$. Defining $\Delta L_{\rm BH}$ to be the fraction of the accretion luminosity emitted at the galaxy center that interacts with the galactic hot gaseous halo, from equation (A10) we obtain

$$\frac{\Delta L_{\rm BH}}{L_{\rm BH}} \simeq \frac{2\sqrt{\pi}\,\Gamma[(b-1)/2]}{\Gamma(b/2)}\frac{n_{\rm e}}{n_{\rm T}}\frac{C_{\rm X}k_{\rm B}T_{\rm X}}{m_{\rm e}c^2}\sigma_{\rm T} n_0 r_{\rm gas} \simeq 3\times 10^{-14} T_{\rm X} n_0, \tag{4}$$

having for simplicity assumed a gas temperature T much lower than the temperature $T_{\rm X}$ associated with the spectral distribution of $L_{\rm BH}$ (see equation [10]), $r_{\rm gas} = 300$ pc, and $b = 2$. For example, for $n_0 = 10^2$ cm^{-3} (a common density value in the central regions of cooling flows, see, e.g., CDPR), and $T_{\rm X} = 10^9$ K, we find a total absorption of 3×10^{-3}, in accordance with that given by

BT95. So, combining equations (3) and (4), we see that we can expect major degassing or strong intermittencies in the accretion (and in the coronal $L_{\rm X}$ evolution as well) when

$$T_{\rm X} \gtrsim 5 \times 10^{-4} \frac{L_{\rm B}\sigma_{\circ *}^2 (1+\mathcal{R})}{n_0 \epsilon \dot{M}_{\rm BH} t_{15}^{1.3}} \approx 3.3 \times 10^7 \frac{\sigma_{\circ *}^2 (1+\mathcal{R})}{n_0 \epsilon} \quad {\rm K}. \tag{5}$$

One can easily imagine situations so that the r.h.s. of equation above is as low as 10^6 K or as high as 10^9 K. This shows at once that the emitted radiation is effective in producing a strong feedback on the accretion flow, but that numerical simulations are needed in order to understand the flow evolution in specific cases. Note here that, for a given value of $\dot{M}_{\rm BH}$ the absorption of energy in the ambient gas is proportional to *both* the efficiency, ϵ, and the Compton temperature $T_{\rm X}$. Thus, so long as $T_{\rm X} >> T_{\rm gas}$, *the basic assumption of this paper*, all that matters is the product $\epsilon T_{\rm X}$ and we will be free, in the work that follows to imagine $T_{\rm X}$ reduced by a factor of ten and ϵ increased by the same factor. We will test this scaling in Section 4.2.4.

A more complex situation may however arise, if the accretion happens onto an accretion disk, and so it may be that much of the emitted radiation is funneled into a small solid angle, so that it is not seen by the inflowing gas, i.e., the assumption of spherical symmetry is qualitatively in error. As a consequence, only a fraction of the surrounding galactic hot gas can see the emitted radiation. We have to remember, hovever, that the nearly isotropic *Thomson* scattering on the electrons can back–heat the galactic gas. One can estimate the order of magnitude of this effect reducing $\Delta L_{\rm BH}$ as given in equation (4) by a fiducial factor $1 - \exp(-\tau) \simeq \tau$, where $\tau = \sigma_{\rm T} \int_0^\infty n_{\rm e}(r) dr$ and only the back–scattered radiation is permitted to heat the ISM. Allowing for this further reduction in the efficiency of the Compton pre–heating on the gas flows and using the same figures as above for the gas distribution, one finds $\tau = \pi \sigma_{\rm T} n_0 r_{\rm gas}/4 \simeq 0.05$, and so the lower temperature limit increases by a factor of 20. A reasonable interval of $T_{\rm X}$ seems to be still available to produce at least strong intermittencies in the gas flow.

The second problem with a naive use of equation (3) is the fact that the balance between the cooling and the heating of the gas in the central galactic regions can be determinant for the flow evolution. In fact it is important to stress that $\Delta L_{\rm BH}/L_{\rm grav} > 1$ is only necessary for a global galaxy degassing: if the gas is able to radiate efficiently the absorbed energy (perhaps as low energy photons), then it is plausible that only a more or less strong perturbation of the flow in the inner galactic regions will result as a consequence of the accretion. However, a simple estimate of the radiating efficiency of galactic gas flows can be obtained directly from observations. The brightest observed X–ray galaxies are characterized by luminosities $L_{\rm X} \lesssim 10^{42}$erg s^{-1}, and we take this as an upper limit for the gas flows radiating efficiency. This is well below $L_{\rm BH}$ predicted by equation (1), and so the cooling time is longer than the heating time during the most intense accretion events.

The third problem with equation (3) is that it gives the order of magnitude of the *steady* power necessary to expell the gas. On the contrary, it is known that Compton heating can produce strong intermittencies on accretion flows: what is the effect of a strong but *impulsive* heating on

galactic inflows? Only numerical simulations can possibly answer these questions. In any case, from this preliminary and very simple analysis, we can expect that the presence of a massive BH at the galaxy centre will be very significant in modifying the gas flow.

The paper is organized as follows. In Section 2 we describe in detail the models and the input physics, in Section 3 we briefly describe the equations of the problem and the numerical code used for their integration. In Section 4 we describe the numerical results for various choices of the parameters, corresponding to various physical assumptions. Finally in Section 5 we discuss the results and their implications.

2. The Model

2.1. The Galaxy Model

The density distribution of the galaxy models have the same profile as in CDPR, in order to maintains continuity with this previous work and so appreciate better the effect of introducing the feedback of the central BH on the gas flows. A detailed description of how their parameters are fixed in order to reproduce galaxies following the Fundamental Plane relation is given in CDPR. The stars are distributed following a truncated King profile (King 1972)

$$\rho_*(r) = \frac{\rho_{*\circ}}{(1+\eta^2)^{3/2}}, \tag{6}$$

where $\rho_{*\circ}$ is the central stellar density, r_{c*} is the galactic core radius, and $\eta \equiv r/r_{c*}$. This distribution is truncated at the tidal radius $r_t = \delta r_{c*}$ to give a finite galaxy mass. In all the explored models we fix $\delta = 180$. The dark matter halo is described by a quasi–isothermal distribution,

$$\rho_h(r) = \frac{\rho_{h\circ}}{1+\eta^2/\beta^2}, \tag{7}$$

where $\beta \equiv r_{ch}/r_{c*}$, $\rho_{h\circ}$ is the central dark matter density and the tidal radius r_t is assumed to be the same as for the stellar distribution. We define two other dimensionless parameters, namely the ratio between the central densities $\gamma \equiv \rho_{h\circ}/\rho_{*\circ}$, and the ratio between the total masses $\mathcal{R} \equiv M_h/M_*$.

The stellar mass loss rate and the SNIa rate are the main evolving ingredients of these models, and again, for an extensive discussion, we refer to CDPR. Here it is sufficient to recall that in the code the stellar mass losses – the source of *fuel* for the activity of the BH – follow the exact prescriptions of the stellar population synthesys, but for quick calculations the approximation $\dot{M}_*(t) \simeq 1.5 \times 10^{-11} L_B t_{15}^{-1.3}\ M_\odot\ \mathrm{yr}^{-1}$ can be used, where as before L_B is the present galaxy blue luminosity in $L_\odot$. The quantity entering the hydrodynamical calculations is not directly $\dot{M}_*$, but the specific rate of mass return $\alpha_* \equiv \dot{M}_*/M_*$. The SNIa rate is parameterized as $R_{SN}(t) = 0.88 \times 10^{-12} h^2 \vartheta_{SN} L_B t_{15}^{-s}\ \mathrm{yr}^{-1}$, where $h \equiv H_\circ/100$ km s^{-1} Mpc^{-1}. When $\vartheta_{SN} = 1$ and $t_{15} = 1$, the standard SNIa Tammann's rate is recovered (Tammann 1982); we use $h = 1/2$.

Assuming for each supernova event an energy release in the ISM of 10^{51} erg s^{-1}, the energy input per unit time over all the galaxy body is then given by

$$L_{\rm SN}(t) = 7.1 \times 10^{30} \vartheta_{\rm SN} L_{\rm B} t_{15}^{-s} \qquad {\rm erg\,s^{-1}}. \tag{8}$$

Besides energy, supernovae provide also mass. We assume that each SNIa ejects $1.4 M_{\odot}$ of material in the ISM, and so the total specific rate of mass return becomes $\alpha = \alpha_* + \alpha_{\rm SN}$, with $\alpha_{\rm SN}(t) = 1.4\, R_{\rm SN}(t)/M_*$. Finally, each SNIa produces $0.7 M_{\odot}$ of iron. Observationally, the ICM contains $0.01 - 0.02 M_{\odot}$ of iron for every $L_{\odot}$ of the galaxy (star) population of the cluster, with no appreciable trend with cluster richness: in the parmeterization we adopted for the SNIa rate this can be obtained with $\vartheta_{\rm SN} = 1/4$ and $s \simeq 1.6 - 1.7$ (see, e.g., Renzini et al. 1993, and references therein).

2.2. The Central BH

At the onset of the cooling catastrophe a flow of gas is suddenly accreted by the BH, and this produces a burst of energy from the galaxy center. The *instantaneous* bolometric luminosity associated with the accretion is:

$$L_{\rm BH}(t) = \epsilon\, \dot{M}_{\rm BH}(t)\, c^2, \tag{9}$$

where $\dot{M}_{\rm BH}$ – the accretion rate on the BH – is assumed to be *positive* if the flow is accreting, and ϵ is the accretion efficiency, usually spanning the range $0.001 \lesssim \epsilon \lesssim 0.1$. A fundamental ingredient in the treatment of the interaction between the galactic gas flow and the radiation $L_{\rm BH}$ is its (normalized) frequency distribution given by $f_{\circ}(\nu) \equiv \tilde{f}_{\circ}(x)/\nu_{\rm T}$, where $x \equiv \nu/\nu_{\rm T}$ and $\nu_{\rm T} \equiv m_{\rm e} c^2/h$ is the Thomson frequency. We adopt

$$\tilde{f}_{\circ}(x) = \frac{\xi_2}{\pi} \sin\left[\frac{\pi(1-\xi_1)}{\xi_2}\right] \left(\frac{\nu_{\rm b}}{\nu_{\rm T}}\right)^{\xi_1+\xi_2-1} \frac{x^{-\xi_1}}{(\nu_{\rm b}/\nu_{\rm T})^{\xi_2} + x^{\xi_2}}, \tag{10}$$

where $h\nu_{\rm b}$=1 MeV is the spectrum break energy, and $\xi_1 = 0.5$ and $\xi_2 = 0.7$; these values are consistent with the observed spectral indices of X–ray emission spectra of QSOs (see, e.g., Lu & Yu 1999). From the adopted spectral distribution given by equation (10) the Compton temperature is $T_{\rm X} \simeq 10^9$ K (see Appendix A). As noted earlier, we can approximately scale results obtained with this $T_{\rm X}$ to a lower value with corresponding increase in ϵ. Of course, the scaling argument breaks down when $T_{\rm X}$ is lower than the mean gas temperature, and our model cannot be applied: in this case the galactic gas will experience Compton cooling, and this case is briefly discussed in Section 5. Here we present observational evidence supporting our choice of high $T_{\rm X}$ associated with the spectra of some well known AGNs in ellipticals. For example, observations of 3C 273 in the range 150-800 keV by OSSE (McNaron-Brown et al. 1997), show a double slope frequency distribution, with $\xi_1 = 0.62$, $\xi_2 = 0.9^{+1.6}_{-0.6}$, and a break energy of 300 ± 100 keV. These values correspond (with a break energy of 200 keV) to $T_{\rm X} \simeq 9.3 \times 10^8$ K, $T_{\rm X} \simeq 5 \times 10^8$ K, and $T_{\rm X} \simeq 10^8$ K, for $\xi_2 = 0.4$, $\xi_2 = 0.9$, $\xi_2 = 2.5$, respectively. However, the above computation does not include the effect of the

so–called “UV bump” (a common feature in the AGNs spectra), and so a more accurate estimate of $T_{\rm X}$ is obtained by using the spectral distribution over the whole observed energy range. We did this computation for 3C 273, possibly the best observed AGN, with available data over the energy range 6.1×10^{-8} eV – 1.0×10^{9} eV (Türler et al. 1999), and we obtained $T_{\rm X} \simeq 3.2 \times 10^{8}$ K. We note here that when limiting the integration to data below 10 keV (200 keV) we obtain $T_{\rm X} \simeq 1.2 \times 10^{6}$ K ($T_{\rm X} \simeq 5.3 \times 10^{7}$ K). The same computation for 3C 279 (Maraschi et al. 1994) gives $T_{\rm X} \simeq 6.6 \times 10^{8}$ K (whole spectrum, 1.6×10^{-5} eV – 9.9×10^{9} eV), $T_{\rm X} \simeq 5 \times 10^{7}$ K (200 keV cut–off), and $T_{\rm X} \simeq 10^{6}$ K (10 keV cut–off). Finally, for Mrk 421 during quiescence (Macomb et al. 1995), we obtain $T_{\rm X} \simeq 10^{9}$ K (whole spectrum, 1.98×10^{-5} eV – 2.1×10^{12} eV), $T_{\rm X} \simeq 2 \times 10^{8}$ K (200 keV cut–off), and $T_{\rm X} \simeq 3 \times 10^{7}$ K (10 keV cut–off). Note the good agreement of the above results with the $T_{\rm X}$ estimate obtained from the X–ray background. Madau & Efstathiou (1999) found that the average photon energy of the X–ray cosmic background is 31.8 keV, which translates to a $T_{\rm X} \simeq 3 \times 10^{8}$ K: then, if one assumes that the typical redshift of emission was $z = 1 \div 2$, there is another factor of two or three bringing one to the range $T_{\rm X} \simeq 6 \times 10^{8} - 10^{9}$ K. This is interesting, because there is increasing evidence that the origin of the X–ray background (at energies larger than 1 keV) is primarily due to AGN type sources (Mushotzky et al. 2000, Giacconi et al. 2000).

The main effect of the emitted radiation on the galactic gas flows considered in our simulations is the Compton heating (and cooling) of the gas: this is due directly to the central radiation source and indirectly to the recycling of the bremsstrahlung radiation produced by the gas heated to very high temperatures by the BH activity. We consider also the effect of photoionization in changing the cooling function at low temperatures, and finally the heating of cold gas due to the photoionization of hydrogen and helium. At each radius the opacity of the gas to the Compton heating is calculated, using for the electrons the Klein–Nishina cross–section. Obviously, photons do not exchange only energy with the gas, but also momentum, and this leads to the introduction in the momentum equation of hydrodynamics of an *effective gravitational field*, that for $L_{\rm BH}$ greater than the Eddington luminosity can revert the velocity of the gas flow. The treatment used to describe numerically all these physical phenomena is given in Appendix A.

2.3. A Numerical Estimate of $L_{\rm BH}$

A non trivial problem is represented by the numerical treatment of $L_{\rm BH}(t)$, a function of the physical quantities that are necessarily defined only at finite distance from the galaxy center, far from the Schwarzschild radius of the BH. A physically correct boundary condition would be to have some grid points inside the radius $R_{\rm X}$ where the potential energy of the gas (due to the presence of the BH) equals the thermal energy of the gas associated with the Compton characteristic temperature $T_{\rm X}$. A simple calculation shows that

$$R_{\rm X} = \frac{2Gm_{\rm p}M_{\rm BH}}{3k_{\rm B}T_{\rm X}} \simeq 3.5 \times 10^{-10}\frac{M_{\rm BH}}{M_{\odot}} \quad {\rm pc}, \tag{11}$$

a very small scale length when compared to the galactic size; moreover the associated time scale is $t_{\rm x} = R_{\rm X}/v_{\rm X}$, where $v_{\rm X}^2 = GM_{\rm BH}/R_{\rm X}$, and so

$$t_{\rm x} = 9.7 \times 10^{-8}\, M_{\rm BH} \left(\frac{T_{\rm X}}{10^9 {\rm K}}\right)^{-3/2} \quad {\rm yr} \tag{12}$$

of the order of ten years for a for $M_{\rm BH} = 10^8 M_\odot$. Clearly these figures prevent the possibility of simulating the gas flow from inside $R_{\rm X}$ to hundreds of kpc over time scales of Gyrs. The problem becomes even worse during the flaring activity: numerical models, in which we calculated the evolution of the gas flow in a region extending up to few parsecs from the BH, and in which 10 grid points are contained inside $R_{\rm X}$, frequently show that the Courant time and the heating time become of the order of a *day*, unequivocally forbidding any attempt of a global numerical simulation extending to all the characteristic temporal and spatial scales. In a subsequent paper we investigate at very high (spatial and temporal) resolution the gas flow close to the BH, i.e., we give a complementary analysis of the problem investigated in this paper, on time scales of the order of years and less. Here we are interested in the behavior of the gas flow on galactic scales and over times of Gyrs, and we believe we have captured with our description the macroscopic properties of the evolution.

We circumvent the problem of obtaining in a consistent way $L_{\rm BH}(t)$ from the hydrodynamical quantities at the first grid point exploring two limiting cases for the description of the accretion. In the first case, that we call *instantaneous* accretion, after a time delay equal to the free–fall time from the first grid point, the inflowing gas is accreted from the BH and disappears in the central sink. For the adopted galaxy model $t_{\rm ff}$ can be easily computed for $r < r_{\rm c*}$:

$$t_{\rm ff}(r) = \sqrt{\frac{3}{4\pi G\rho_{*\rm o}(1+\gamma)}} \int_0^1 \frac{\sqrt{x}\, dx}{\sqrt{(1-x)(\mathcal{D}+x+x^2)}}, \tag{13}$$

where $\mathcal{D} = 3M_{\rm BH}/2\pi\rho_{*\rm o}(1+\gamma)r^3$. The integral can be evaluated explicitly in terms of elliptic functions, and equals $\pi/2$ for $\mathcal{D} = 0$ and $\pi/3$ for $\mathcal{D} = 1$. For $\mathcal{D} \to \infty$ the integral is asymptotic to $\pi/2\sqrt{\mathcal{D}}$.

In the second case, which we call *smoothed* accretion, we mimic the presence of an accretion disk around the BH, where the fuel is stored during the inflow phases and subsequently released on the BH. In our spherically symmetric models, this complex phenomenon is simply simulated introducing the *accretion time*, $t_{\rm accr}$, in which the gas from the accretion disk disappears in the BH. With this assumption a given amount of gas that crosses the first grid point at the time t is not accreted instantaneously at $t + t_{\rm ff}$ but with an exponential decay of characteristic time $t_{\rm accr}$. For example, in the α–disks, $t_{\rm accr} = O(t_{\rm orb}/\alpha)$, where $t_{\rm orb}$ is the orbital time at that radius (Shakura & Sunyaev 1973). We use the parametrization $t_{\rm accr} = \kappa t_{\rm x}$, and the method used for the numerical computation of $L_{\rm BH}(t)$ in this case is described in Appendix B.

Obviously for a fixed efficiency and for a given quantity of accreted mass the *energy* released in the two scenarios is the same, and so the *luminosity* produced by the smoothed accretion is

lower but emitted over a longer time (a few $t_{\rm accr}$). What may be the effect of a smoothed accretion on a short time–scale is not hard to imagine: in fact, it is natural to expect a *reduced* effect on the gas flow with respect to the instantaneous accretion model with the same efficiency ϵ. In other words, we expect something similar to a reduction of the *effective* efficiency. Over longer time–scales a guess on the gas behavior is not so simple: from the reduction of $L_{\rm BH}$ one would expect the flow to become more similar to that with instantaneous accretion and smaller ϵ, i.e., a more uniform flaring activity possibly without a major galactic degassing. But it is also true that after few $t_{\rm accr}$, the energy emitted is the same as in the case of the instantaneous accretion. This smoother energy release over a longer time could produce a *stronger* tendency to global degassing. Only numerical simulations can answer which of these two competing effects will finally dominate.

3. The Hydrodynamical Equations

As in CDPR, the evolution of the galactic gas flows is obtained integrating the time–dependent Eulerian equations of hydrodynamics with source terms:

$$\frac{\partial \rho}{\partial t} + \nabla \cdot (\rho v) = \alpha \rho_*, \tag{14}$$

$$\frac{\partial m}{\partial t} + \nabla \cdot (m v) = -(\gamma - 1)\nabla E + g_{\rm eff}\rho, \tag{15}$$

$$\frac{\partial E}{\partial t} + \nabla \cdot (E v) = -(\gamma - 1)\, E \nabla \cdot v - L_{\rm r} + L_{\rm h} + \alpha\rho_*(\mathcal{E}_\circ + \frac{1}{2}v^2), \tag{16}$$

where ρ, m, and E are respectively the gas mass, momentum and internal energy density, and v is the gas velocity. The ratio of the specific heats is $\gamma = 5/3$, and $g_{\rm eff}(r)$ is the effective acceleration experienced by the gas, considering the effect of the radiation field (see Appendix A). $\mathcal{E}_\circ = 3k_{\rm B}T_\circ/2\mu m_{\rm p}$ is the injection energy per unit mass, where $T_\circ(r,t) = [\alpha_{\rm SN}(t)T_{\rm SN} + \alpha_*(t)T_*(r)]/\alpha(t)$ is the gas injection temperature, that describes the heating of the gas by the thermalization of the SNIa blast waves and of the stellar mass losses due to their relative motion with respect of the ISM. $T_{\rm SN}$ is obtained as in CDPR, while the injection temperature due to the stellar random motions $T_*(r) \equiv \mu m_{\rm p}\sigma_*^2(r)/k_{\rm B}$ is increased near the galaxy center with respect to the models discussed in CDPR, due to the the presence of the BH. The radial behavior of the stellar velocity dispersion can be explicitly found for the King density distribution by solving the Jeans equation:

$$\rho_*(r)\sigma_*^2(r, M_{\rm BH}) = \rho_*(r)\sigma_*^2(r, M_{\rm BH}=0) + \frac{GM_{\rm BH}\rho_{*\circ}}{r_{\rm c*}}\left[\frac{1+2\eta^2}{\eta\sqrt{1+\eta^2}} - \frac{1+2\delta^2}{\delta\sqrt{1+\delta^2}}\right], \tag{17}$$

where for simplicity we assumed global isotropy of the velocity dispersion tensor. The first term on the r.h.s. of equation (13) is the velocity dispersion without the BH (see, e.g., Ciotti 1993). In the energy equation $L_{\rm r}$ is the cooling function, modified to allow for the ionizing effects of $L_{\rm BH}$ on the cold gas, and the total heating function is $L_{\rm h} = L_{\rm C} + L_{\rm ph} + L_{\rm Br}$. $L_{\rm C}$ is the Compton heating

(or cooling), $L_{\rm ph}$ describes the effect of the photoionization heating on hydrogen and helium, and finally $L_{\rm Br}$ describes the effect of recycling the bremsstrahlung radiation emitted from the inner part of the galaxy on the external part of the gas flow. A detailed discussion of the heating and cooling functions is given in Appendix A.

The numerical engine of the code is essentially the same as in CDPR, i.e., a first order, eulerian up–wind scheme (van Leer 1977), on which several gestures towards second order accuracy are implemented. In the computation of galaxy models the grid has 120 zones and extends up to 500 kpc. In order to obtain an acceptable spatial resolution in the inner regions a geometrical progression for the mesh size is adopted. At the outer boundary the usual outflow conditions are assumed. The first active grid point for the discussed models is placed at 20 pc from the galaxy center, and this, at variance with what was done by BT95, is an *active* grid point, in the sense that the fluid velocity is self–determined by the flow and by the heating during the flare activity, and not imposed as a boundary condition. Some models were run with higher resolution, i.e., with the first active grid placed at 10, 5, or 2 pc from the center, obtaining a good qualitative agreement of the resulting evolution with that obtained using the larger grid.

The sink of the hydrodynamical quantities due to the BH is simulated by removing inside the first grid point the equivalent quantity of density, momentum, and energy that disappears during the accretion events. We assume the model galaxies to be initially devoid of gas, i.e., $\rho(r) = 0$ for $t = 0$. This is certainly a simplification of the real physical situation in the early evolutionary stages of elliptical galaxies, when intense star formation takes place. In this way only the gas originated by stellar mass loss is actually considered. Our initial condition, $\rho(r) = 0$, is therefore equivalent to assuming that galactic winds are established by SN activity (mainly type II), early in the evolution of elliptical galaxies. The choice of the time–step is determined by five characteristic time–scales related to different aspects of the problem: the Courant time $t_{\rm C}$, the cooling time $t_{\rm r} = E/L_{\rm r}$, the density source time $t_{\rm d} = \rho/|\dot{\rho}|$, the heating time $t_{\rm h} = E/L_{\rm h}$, and finally the free–fall time from the first grid point, $t_{\rm ff}$. The numerical time–step is taken to be some specified fraction (0.5 or less) of the minimum of the previous times computed over the integration grid, and the equations are integrated using the time–splitting method.

4. The Results

In this Section we present the results of the simulation of the gas flow for a model similar to model KRM discussed in CDPR. For this reference model we adopt $L_{\rm B} = 5\times10^{10}L_\odot$ and $\sigma_{\circ *} = 280$ km s^{-1}, obtaining from the FP relation $R_{\rm e} = 4.2$ kpc (and so $r_{{\rm c}*} = 350$ pc, $\rho_{*\circ} = 7.15 \times 10^{-19}$ g cm^{-3}, and $M_* = 2.8 \times 10^{11} M_\odot$, see CDPR). The dark matter halo is characterized by $\mathcal{R} = 7.8$ and $\gamma = 1.25 \times 10^{-2}$ from which $\beta = 4.2$. The BH accretion efficiency is assumed to be $\epsilon = 0.1$, and for the SNIa parameters we adopt $(\vartheta_{\rm SN}, s) = (2/3, 1.5)$, a choice for which initially there is ample SN heating to sustain a supersonic wind. The accretion mechanism adopted for this model is instantaneous accretion, and the free–fall time from the first grid point (20 pc) is $t_{\rm ff} \simeq 1.5 \times 10^5$

yr. In Table 1 all the model parameters, together with the derived quantities, are reported (model #1). Above it, we show the properties of model #0, which is identical to model #1, except that all feedback is turned off; the assumed efficiency is $\epsilon = 0$. We note here that the expected present day iron abundance in the gas flow of this model would be $\simeq 4.3$ times the iron solar abundance, considerably larger than the current observational estimates. However, we present here this model in order to have a direct comparison with the same model discussed in CDPR; moreover, in Sections 4.2.3 and 4.4 we present other models with a reduced SNIa rate.

In the following Subsections we will explore the changes in the characteristics of the evolution by decreasing the efficiency ϵ from the reference value (0.1) to 0.01 and 0.001, by increasing the dark–halo mass to reduce the time $t_{\rm cc}$ of the global cooling catastrophe or decreasing the SNIa rate, and finally by mimicking in a qualitative way the effect of the presence of an ADAF solution or optically thick accretion disk in the galaxy center.

4.1. The Evolution of Model #1

A common characteristic of all models discussed in this paper is obviously their similarity with WOI models up to $t_{\rm cc}$, a substantial central activity starting only after the onset of the cooling catastrophe. For this reason here we do not describe in detail the flow evolution before $t_{\rm cc}$, which the interested reader can find in CDPR, where the three main phases of *wind*, *outflow*, and *inflow* are exaustively discussed. In this paper we concentrate instead on the evolutive phases for $t > t_{\rm cc}$, discussing the previous evolution only where necessary to understand the new results presented. We parenthetically note that the wind and outflow phases are required if one is to understand the high metal content of gas in cluster of galaxies (see also Section 4.4).

In Fig.1ab the time evolution of the mass budget of model #1 is shown, sampled at time intervals of 1 Myr. More specifically, in Fig.1a the dotted line represents the mass of gas, $M_{\rm gas}(t)$ in solar masses contained inside the galaxy truncation radius $r_{\rm t} = \delta r_{\rm c*} = 63$ kpc, and the solid line the mass accreted on the BH, $M_{\rm sink}$. In Fig.1b, the *rates* of variation of various masses are shown, all in solar masses per year: the dotted line represents the mass return from the stellar population $\dot{M}_*$, the dashed line the rate of mass loss at the tidal radius $\dot{M}_{\rm out} = 4\pi r_{\rm t}^2 \rho(r_{\rm t}) v(r_{\rm t})$, and the solid lines is the accretion rate on the BH, $\dot{M}_{\rm BH}$. The temporal evolution of these quantities is easily understood. During the early *wind* phase the flow is characterized by supersonic outward velocities driven by SNIa heating, and more gas is lost at $r_{\rm t}$ than produced inside the galaxy by the stellar population. The wind phase ends due to the decreasing of the specific heating, that smoothly leads to the *outflow* phase, i.e., to a subsonic degassing. However, a time comes when the outflow velocity has decreased so much that the internal gas density begins to rise, in spite of the continuing decrease in $\dot{M}_*$. Correspondingly, the total amount of gas inside the galaxy reaches a minimum precisely when the rate of mass loss from the galaxy drops below the rate of injection of fresh gas $\dot{M}_*$. In model #1 this minimum is reached at ~ 5 Gyr, as can be clearly seen in Fig.1a.

In Fig.1c the flow evolution is seen from an energetic point of view: the short–dashed and long–dashed lines are respectively the power supplied to the gas by the SNIa explosions ($L_{\rm SN}$, equation [8]), and the power required to *steadily* extract from the galaxy potential well the gas lost by the evolving stellar population ($L_{\rm grav}$, equation [2]). The solid line represents the coronal X–ray luminosity of the gas, $L_{\rm X}$, that would be observed in the 0.5–4.5 keV range. Note how up to $t_{\rm cc}$ the time evolution of $L_{\rm X}$ follows strictly that of the gas mass inside the galaxy. Superimposed is the luminosity produced by the accretion, as given by equation (1).

Returning to a discussion of the gas flow, we see that, as more and more gas builds up inside the galaxy, its central density rises, the radiative losses become increasingly more important, a smaller fraction of the SNIa heating is left to drive the flow, and in turn the flow deceleration causes a faster increase of the gas density. Inevitably, a moment comes when, at the center, the heating rate drops below the cooling rate, and a central cooling catastrophe suddenly reverses the direction of the flow in the inner region of the galaxy: the transition to an inflow regime is virtually instantaneous. In the models described in CDPR this phase was called *inflow*, and after this point the evolution of their models is smooth, as can be seen in Fig.2, where $L_{\rm X}(t)$ of a model identical to model #1 but without the central BH is shown (dotted line, model #0 in Table 1) superimposed to that of model #1 (solid line). The value of the time averaged X–ray luminosity $< L_{\rm X} >$ is slightly below 10^{41} erg s^{-1}, comparable with typical observed X–ray bright ellipticals (see Table 2). In comparison, model #0 (without feedback) has an average luminosity of 10^{42} erg s^{-1}, considerably above observed sources.

For the specific choice of parameters made for model #1, the cooling catastrophe happens at $t_{\rm cc} \simeq 9$ Gyr, when negative infall velocities appear near the center, and rapidly exceed ~ 100 km s^{-1} at a few hundreds pc away from it. From this time onwards the flow evolution is substantially altered by the presence of the BH with respect to the models discussed in CDPR. Immediately after $t_{\rm cc}$ an accretion rate of $\dot{M}_{\rm BH} \gtrsim 100\ M_{\odot}{\rm yr}^{-1}$ is established, as can be seen from Fig.1b (and its time expansion in Fig.3a). The accretion on the BH produces a strong energetic feedback, the gas in the central regions of the galaxy is heated by the emitted radiation approximately to the Compton temperature $T_{\rm X}$, and as a consequence it starts to expand and its density decreases by orders of magnitude. The effect of this strong heating near the BH is a correspondingly strong reduction of the gas radiative losses, and the accretion on the BH suddenly stops: only after an episode of local cooling can the next accretion event take place, and the cycle re–starts. When the amount of accreted gas is sufficient, a strong shock wave finally reaches the galactic tidal radius, reducing dramatically the amount of the total gas present inside the galaxy. Only after the time required for the stellar mass losses to replace the gas lost, can the gas density increase sufficiently for the radiative losses to become again important over galactic scales and produce a new cooling catastrophe. During brief periods the central BH emits in the range $10^{46} \gtrsim L_{\rm X}/{\rm erg\,s^{-1}} \gtrsim 10^{45}$, compatible with typical AGN luminosities.

The described evolution can be followed from a local point of view in Fig.1d, where the evolution of the gas (number) density (dotted line) and temperature (solid line) at the inner active

grid point (20 pc) is shown. All the discussed phases can be easily recognized: particularly note how $\dot{M}_{\rm out}$ soon after each accretion event overcomes $\dot{M}_*$, so decreasing the total amount of gas inside the galaxy. From Fig.1a one can also note how the total amount of mass which has been accumulated by the BH after 15 Gyr is relatively low and compatible with typical luminous AGN, only $\sim 10^8 M_\odot$: on the contrary, the same model without the central BH (model #0), whose $L_{\rm X}$ is represented in Fig.2 with the dotted line, at $t = 15$ Gyr had accumulated in its central regions more than $\simeq 1.5 \times 10^{10} M_\odot$ of gas, more than observed in any purported central BH.

As in the case of the evolutionary phases preceeding the cooling catastrophe, namely the wind and the outflow phases, also during the AGN–like phases the coronal X–ray emission of the gaseous halo follows the evolution of the mass of the gas inside the galaxy, as can be seen in Fig.1c, where the solid line is $L_{\rm X}$. The dotted line in the same figure is $L_{\rm BH}$, and it is interesting to observe how $L_{\rm X}$ and $L_{\rm BH}$ are anti–correlated: during the accretion phases the total luminosity is completely dominated by the nuclearly concentrated $L_{\rm BH}$, on the contrary during the quiescent BH phases the galaxy emission is due only to the hot gas $L_{\rm X}$, and so it is diffuse as observed in X–ray elliptical galaxies. As a consequence, the luminosity evolution of model #1 is composed by two spatially and temporally complementary phases, characterizing the two different flow regimes: one, very short, in which the total luminosity is dominated by the central activity, and another, much longer, dominated by the coronal gas diffuse luminosity. Observationally, we would identify one phase with AGNs and the other with nascent cooling flows.

The temporal evolution of $L_{\rm X}$ is shown in Fig.2 (solid line) where one see also its large excursion (even more than a factor of 100) from immediately after the nuclear bursts compared with before the accretion events. A very important parameter characterizing the different phases of the galaxy luminosity evolution is the duty cycle $f_{\rm BH}$ of the central engine, that we define as[3]

$$f_{\rm BH} \equiv \frac{(\int_{t_{\rm cc}}^{15} L_{\rm BH}\, dt)^2}{(15 - t_{\rm cc}) \int_{t_{\rm cc}}^{15} L_{\rm BH}^2\, dt}. \tag{18}$$

For model #1, we found $f_{\rm BH} \simeq 10^{-4}$; thus this model would be seen as an AGN for only a very small fraction of the Hubble time.

A final comment on the global $L_{\rm X}$ evolution is in order to stress how an intrinsic mechanism able to produce a large scatter in the diffuse X–ray luminosity of ellipticals is naturally available when a strongly discontinuous nuclear activity is present: statistically the X–ray observations can catch $L_{\rm X}$ in any point of its variation, and this variation, as can be clearly seen in Fig.2, can be as high as the variation during the wind and outflow phases. A discussion of this point is postponed in Section 5.

We move now to describe the small–scale temporal evolution of the accretion events. In fact,

---

[3]Note that for a burst of time duration Δt_b and constant luminosity, $f_{\rm BH} = \Delta t_b/(15 - t_{\rm cc})$; it is the fraction of time that the BH is "on". For a luminosity profile $L(t) \propto A - \cos(\omega t)$ and $A \geq 1$, $f = 2A^2/(1 + 2A^2)$.

as can be seen from Fig.1, each burst shows a rich temporal sub–structure that is interesting to discuss in greater detail.

In Fig.3abc we plot the temporal expansions of the corresponding panels in Fig.1bcd, sampling the represented quantities at time intervals of 10^4 yr. In Fig.3a the instantaneous accretion rate is shown, and its sub–structure is apparent: these short–time intermittencies, of increasing intensity, are due to reflected shock waves in the inner regions of the galaxy that carry fresh gas to the BH. After many of these precursors a larger amount of gas is finally accreted, and the galaxy can effectively lose a significative fraction of its gaseous halo, with ejection velocities at $r_{\rm t}$ of the order of 100 km s^{-1} or more. The relative role of cooling and heating is apparent in Fig.3c.

A very small but representative sample of the radial profiles of the hydrodynamical quantities at various important evolutionary phases is shown in Fig.4. In the right column the gas flow is approaching $t_{\rm cc}$: each line is separated by the successive (in the following order: solid, dotted, short-dashed, long-dashed, dotted-dashed) by 10 Myrs, starting at 9.01 Gyrs. Thedetailed description of this phase (the end of the outlfow phase in WOI models) is given in CDPR.

The three panels of the central column cover the evolution of the flow in the time interval 9.06-9.10 Gyrs, i.e., during a period of strong instabilities (as can be seen from Fig.3c). Note how large (i.e., supersonic) positive and negative velocities are present well inside the effective radius, and how cold shells carry new fuel to the central BH: one of such events can be seen following the cold shell represented by the dotted line, and after that the short dashed line showing a low density cavity expanding at high velocity. Soon after another dense shell forms and falls on the center (dotted-dashed line). Sometimes, outward moving blast waves catch up to previous blast waves, and reflect back.

Finally, in the last column, the time sequence starts after a considerable accretion event, at 9.2 Gyr (see Fig.3c). The emitted energy is able to "clean" the central galactic regions: the perturbations propagate towards the galactic tidal radius, and the density profile returns smooth (and characterized by a well defined, centrally flat, low density profile).

As already pointed out in the Introduction, we allowed in our simulations for the effects of the gas opacity and photoionization heating. For model #1 it turns out that the fraction of $L_{\rm BH}$ trapped by the hot gas around the galaxy never exceeds 10^{-2}, and many times reaches values as low as 10^{-4}, confirming the estimates obtained in the Introduction and by BT95. We conclude that the gas is always optically thin, but nevertheless we performed all simulations using the correct treatment for the opacity. Moreover, the same model with and without photoionization heating (as well as *all* models we explored) produced essentially the same evolution. We collect in Table 1 the relevant overall properties of model #1, to be compared with variant models. Comparison between model #0 and the others shown makes clear that a feedback effective efficiency even as low as $\epsilon\tau = 10^{-3} \times 10^{-3} = 10^{-6}$, is enough to radically change the outcome from the zero feedback case.

4.2. Exploring the Parameter Space

We move now to comment on some models in which the basic parameters (efficiency, dark matter amount, SNIa rate, Compton temperature) are changed with respect to model #1. Actually, we computed many more models than those discussed in the following, but those presented can be considered a representative set of the various kinds of evolution we found.

4.2.1. Reducing the Efficiency

In this Section we describe the effects on model #1 gas flow by assuming now $\epsilon = 0.01$ and $\epsilon = 0.001$ (labelled models #2 and #3). These two models are also explored in the scenario of istantanous accretion. The evolution for $t < t_{\rm cc}$ is the same already discussed, and so we start our description directly at $t = t_{\rm cc}$, expecting that a reduction in the efficiency will lead to a flow evolution in which the probability of major degassing events is reduced if not impossible. As discussed in the Introduction this does not also mean that the central, short–time bursts disappear: on the contrary, it is possible that now a *greater* fraction of the flow evolutionary time is spent at high $L_{\rm BH}$, with the consequent increase of $f_{\rm BH}$.

For $\epsilon = 0.01$ (model #2), the model evolution is qualitatively similar to model #1, as can be seen from the value of the various quantities given in Table 1. Note that the total mass accreted by the BH has increased now to $3.1 \times 10^8 M_\odot$, due to the lower efficiency that produces a weaker feedback on the gas flow for the same mass accretion rate.

The same trend is also shown by model #3, where $\epsilon = 0.001$: in fact, at 15 Gyr the BH mass is increased by $\sim 4.3 \times 10^8 M_\odot$, and more bursts are present. For what concerns the BH duty cycle, we found $f_{\rm BH} = 2.7 \times 10^{-4}$ and $f_{\rm BH} = 3.8 \times 10^{-4}$, for model #2 and #3, respectively. However, notwithstanding these differences, the temporal structure of the luminosity evolution of these three models remains qualitatively the same, as can be seen comparing the three panels in Fig.5, where the energetic of models #1,2,3 is shown. Even for these two latter models the total fraction of trapped $L_{\rm BH}$ in the hot gas remains very low during all the evolution, with values in the range $10^{-4} - 10^{-3}$. Relevant overall properties of models #2 and #3 are displayed in Table 1. Especially to be noted is the relatively small range in the mean gas X–ray luminosity $< L_{\rm X} >$. As the efficiency is reduced by two orders of magnitude $< L_{\rm X} >$ increases from 7.6×10^{40} erg s^{-1} to 1.5×10^{41} erg s^{-1}, all values being far below the no feedback value of $\simeq 10^{42}$ erg s^{-1} (model #0, see Table 2).

4.2.2. Early Cooling Catastrophe: Increasing the Dark Matter Content

In this Section we describe the results obtained for the evolution of three models correspondingly identical to models #1,2,3 in their stellar amount and accretion efficiencies

($\epsilon = 0.1$ in model #4, $\epsilon = 0.01$ in model #5, and $\epsilon = 0.001$ in model #6), but in which the dark matter to visible matter mass ratio is increased from 7.8 to 10, in order to obtain an earlier cooling catastrophe. As a consequence, $t_{\rm cc}$ decreases from ~ 9 Gyr to ~ 4.2 Gyr.

In the three models, the luminosity evolution is of the same type of that presented by model #1, but the central energy bursts are much more frequent (see Fig.6). This is a direct consequence of the fact that now the galaxy potential well is deeper with respect to that of model #1, as qualitatively shown by equation (3); moreover, as in models with reduced efficiency described in Section 4.2.1, the probability of major degassing events is reduced if not impossible. Thus, the total mass accreted by the BH in these models is higher than in the corresponding cases with less massive dark haloes: in fact, we found values of $5.8 \times 10^8 M_\odot$, $7.0 \times 10^8 M_\odot$, and 6.9×10^8, for models #4,5,6, respectively. Note however that a model without feedback and identical in all other properties to models #4,5,6, accretes on its central BH $\Delta M_{\rm BH} = 2.5 \times 10^{10} M_\odot$ over an Hubble time. The same comment applies to the duty cycle, for which we found $f_{\rm BH} = 2.1 \times 10^{-4}$, 2.6×10^{-4}, and 2.5×10^{-4}, for models #4,5,6, respectively. It is interesting to note that the model presenting the strongest tendency towards global degassing is *not* model #4 (the model with the higher efficiency), but model #5 (with $\epsilon = 0.01$). This is also the model that accreates more mass, and with the higher duty–cycle. Relevant overall properties of these models are displayed in Table 1.

4.2.3. Early Cooling Catastrophe: Reducing the SNIa Rate

As anticipated in the Introduction, one of the main objections raised against the WOI scenario is the claimed detection of low iron abundance in the ISM of ellipticals. Prompted by this fact, we also present three models (models #7,8,9) in all respects identical to models #1,2,3, except for the fact that now $\vartheta_{\rm SN} = 1/4$ instead of $2/3$ (see equation [8]). Moreover, we also computed three more models identical to models #7,8,9, but with the ratio between the dark matter halo mass to stellar mass reduced from 7.8 to 3 (models #10,11,12). Others models analogous to models presented in this Section, but with a smaller $L_{\rm B}$ and central velocity dispersion, are described in Section 4.4.

With the reduction in the SNIa heating, the cooling catastrophe happens now at $t_{\rm cc} = 0.25$ Gyr. For the three explored efficiencies, the effects on the temporal behavior of the bursts are dramatic: the separation between the long phases of quiet evolution and the short bursts with rich temporal sub–structures chracterizing model #1 is practically disappeared, and only a very strong BH activity is present, with some intervals during which a more global degassing is approached. Very few and short outgassing events are still present, but the time between successive major accretions is substantially reduced. This is shown in the upper panel of Fig.7, where the luminosities are plotted in the representative time interval from 9 Gyr to 9.5 Gyr, for model #7 ($\epsilon = 0.1$): because of this the qualitative aspect of the evolution of the flow remains of this kind over all the evolution for the three models.

As stressed above, the temporal sub–structure of the accretion is maintained, i.e., the accretion is still locally unstable. This fact is rich in consequences, the most important of which is the increase of duty cycle, with respect to models with "late" cooling catastrophe: in fact, now $f_{\rm BH} = 1.5 \times 10^{-3}$, 1.8×10^{-3}, and 1.6×10^{-3} for models #7,8,9. Moreover, the total mass accreted by the BH in these three models is $3.5 \times 10^9 M_\odot$, $4.9 \times 10^9 M_\odot$, and 5×10^9, respectively, substantially higher than in the models previously presented. For comparison, we computed also the mass accreted on the central BH by an identical model with $\epsilon = 0$, and we found $\Delta M_{\rm BH} \simeq 2.5 \times 10^{11} M_\odot$, even higher (as expected) than our first computed no feedback model #0.

The behavior of models #10,11,12 is very similar, and their relevant properties are listed in Table 1; again, for the corresponding model with $\epsilon = 0$, it turns out that $\Delta M_{\rm BH} \simeq 1.1 \times 10^{11} M_\odot$. From the values reported in Table 1 one can see how the decrease of the ratio $M_{\rm h}/M_*$ (maintaining all other model parameters fixed) produces a reduction of the total mass accreted by the BH (cfr. also models #1,2,3 with #4,5,6). As illustration, the luminosity evolution of model #10 is shown in Fig.7 (middle panel).

4.2.4. Reducing $T_{\rm X}$

As anticipated in the Introduction, a simple argument suggest that models with constant $\epsilon T_{\rm X}$ should behave in the same way, so long as $T_{\rm X} >> T_{\rm gas}$. In order to test quantitatively this prediction, we computed a few models with the Compton temperature reduced by a factor of 10: models #1r and #2r are derived from models #1,2 assuming $T_{\rm X} = 10^8$ K, and in model #1rr $T_{\rm X} = 5 \times 10^7$ K. The resulting evolution is very similar to that of previous models, so that even substantial reductions of the Compton temperature (as long as $T_{\rm X}$ is higher than the mean gas temperature) produce a strongly unstable evolution. The overall properties of these models are presented in Table 1. The first apparent result is that, as expected, the central BH of each "temperature reduced" model accretes more mass than the corresponding "hotter" model. However, the scaling is not perfect. This is due to the complex nature of accretion. In fact, as discussed in Section 4.1, each accretion event is made of two different dynamical phases. In the first, the accretion is determined by the cooling of gas, and the scaling argument perfectly applies. The second phase, (where a substantial fraction of the gas is actually accreted) is characterized by many accretion events (with a substantially lower accretion rates) caused by reflected shock waves propagating in the central region of the galaxy. After the first, cooling dominated accretion event, the gas temperature in the central regions of the galaxy can reach values as high as 10^9 K, and so the scaling argument no longer applies rigorously. For example, computing the *mean* accretion gas temperature at the first grid point (20 pc) for a complete accretion event in model #1r we found

$$\frac{T_{\rm X}}{< T_{\rm gas} >} \equiv \frac{\int \dot{M}_{\rm BH} T_{\rm X}/T_{\rm gas}\, dt}{\int \dot{M}_{\rm BH}\, dt} \simeq 1.9. \tag{19}$$

Moreover, approximately 2 per cent of the total mass accreted by the central BH in the accretion event is at temperature *higher* than $T_{\rm X}$, i.e., in Compton cooling regime. This explain the semingly

counterintuive result that the total mass accreted by these models with reduced T_X *decreases* with decreasing efficiency, at variance with all the other models: obviously the effect of Compton cooling is stronger for the higher efficiency models. In any case, the main features of all the other models are retained: the time spent by the galaxy in a AGN state is still very small, the accreted mass is low, and the time averaged $< L_X >$ is substantially lower than that of model #0 (see Table 2).

4.3. Non–Spherical Accretion: ADAF and Optically Thick Accretion Disks

The assumption of spherical symmetry adopted in our models is certainly not realistic for an accurate modelling of the accretion phenomenon. This is specially true near the BH, where, in the case of a non–zero angular momentum, the gas can be stored in an accretion disk, and then smoothly released with some characteristic time scale on the BH. Another interesting possibility recently suggested is the so–called *Advection Dominated Accretion Flow* (see, e.g., NY95), where the resulting efficiency can be very low, due to nature of the solution (radiation from relatively low density gas, see Park & Ostriker 1999, and references therein). Certainly the answer to this problem can be obtained only using at least a 2D numerical code (in the interior parts of the flow), but despite this obvious limitation, we believe that some very simple numerical experiments can be of some real interest. In fact, given the relatively low specific angular momentum assumed in the ADAF solutions, they would be quite spherical in the domain explored by our simulations ($r \geq 20$ pc). Thus our computations plausibly represent the feeding (outer boundary condition) for the ADAF models.

4.3.1. ADAF

We start by presenting the results of a simulation in all ways similar to model #1, but where we replaced the central engine with the mildly unspherical ADAF solution. Following NY95, we modify $L_{\rm BH}$ as

$$L_{\rm BH}(t) = \frac{\dot{m}}{\alpha^2 + \dot{m}} \epsilon \dot{M}_{\rm BH}(t) c^2, \tag{20}$$

where we use $\alpha = 0.3$ and $\dot{m} \equiv \epsilon c^2 \dot{M}_{\rm BH}/L_{\rm Edd}$. At low accretion rates the effective efficiency is proportional to $\epsilon\dot{m}$ in the ADAF solution as it is in the equivalent spherical case (Shapiro 1973, Park & Ostriker 1998) but it limits out to ϵ for high $\dot{m}$. Model #13 is analogous to model #1, i.e., $\epsilon = 0.1$, as assumed by NY95. The resulting evolution of this model is characterized, quite surprisingly, by a *more* effective degassing than that showed by model #1. In fact in this case, when the accretion starts, the central BH is *less* reactive than in the analogous model #1, due to the effect of the modulating factor in the equation above. As discussed in Section 2.3, this allows a *larger* quantity of gas to be accreted in any single burst, and as a consequence a stronger effect on the galactic gas flows (see Fig.8, upper panel). The total mass accreted by this model is

$2.1 \times 10^8 M_\odot$, and its duty cycle is $f_{\rm BH} = 1.2 \times 10^{-4}$.

Two more models with the central ADAF, but with the efficiency reduced to $\epsilon = 0.01$ (model #14) and $\epsilon = 0.001$ (model #15), show a reduced tendency towards global degassing. Their duty cycle is now $f_{\rm BH} = 1.3 \times 10^{-3}$ for model #12 and $f_{\rm BH} = 3.3 \times 10^{-3}$ for model #13, and, correspondingly, the total mass accreted by the BH is $4.4 \times 10^9 M_\odot$ and $2 \times 10^{10} M_\odot$. Their luminosity evolution is shown in Fig.8 (middle and lower panel, respectively). Again, the reduction of ϵ produces dramatic consequence on the model evolution, but the flow is still strongly unstable.

Thus, while we stress again the fact that the models here presented can give at best a qualitative understanding of the gas evolution in galaxies, we note that there are compelling evidences that ADAF solutions, *at least when residing in galactic cooling flows*, are unstable to Compton pre–heating. Since the duty cycle is invariably very low, the ADAF ("AGN") flow would be seen only a small fraction of the time, perhaps providing a viable solution to the problem of the apparent lack of QSO activity in most ellipticals.

4.3.2. Optically Thick Accretion Disks

Finally we turn to a substantially different case. To look at a maximally non spherical inner solution we consider the possible presence of physically thin, optically thick accretion disk. Two effects are considered here: the first is the fact that now a substantial fraction of the emitted luminosity $L_{\rm BH}$ can be shielded by the disk and thus emitted in only a narrow cone emanating from the central BH, and, second, the modulation in the accretion due to the storage of the gas in the accretion disk will alter the temporal behavior. As discussed in the Introduction, we model the effect of the disk on the gas heating computing at each time step the Thomson opacity τ of the galactic ISM, and then allowing only the back–scattered fraction, $1 - \exp(-\tau)$, of $L_{\rm BH}$ to be thermalized. As described in Section 2.3, the second effect is characterized by the introduction of the parameter $t_{\rm accr} = \kappa t_{\rm x}$, which prescribes the rate of the fuel release from the disk to the BH. The detailed description of how this release is modeled in the code is given in Appendix B. In these models $\epsilon = 0.1$, as is commonly assumed in accretion disks.

The two models here presented are structurally identical to model #1, and are evolved adopting $t_{\rm accr} = 10^2 t_{\rm x} \simeq 10^3$ yr, and $t_{\rm accr} = 10^4 t_{\rm x} \simeq 10^5$ yr (models #16 and #17, respectively). The resulting evolution was quite insensitive to the exact value of $t_{\rm accr}$, but very much affected by the reduction of the effective Compton heating. In fact, altough strong variability is present (see Fig.7, lower panel, where the luminosity evolution of model #17 is shown), no major degassing events are visible. In both cases the duty cycle, the fractional time during which a quasar would be seen in the center remains small, precisely $f_{\rm BH} \simeq 5.3 \times 10^{-2}$ and 5.4×10^{-2} for models #16 and #17, respectively, but substantially higher than all others duty cycles listed in Table 1. In any case, also for these models, the diffuse gas remains optically thin over all the simulation. The mean X–ray luminosity of the gas in the two models is nearly identical, i.e., $< L_{\rm X} > \simeq 3 \times 10^{41}$ erg

s^{-1}, and the final BH mass is $\simeq 1.6 \times 10^9 M_\odot$.

So, with this small number of models designed to investigate the possible effect of non–spherical accretion, we reached the quite counterintuitive conclusion that, albeit characterized by high efficiency, the optically thick accretion disks are *less* effective than ADAF solutions in expelling the gas from the galaxy potential well. However in both cases the essential results of the spherical case are retained. Only a small fraction of the ambient ISM is accreted to the center with, for the bulk of the gas, the time–averaged Compton heating balancing the radiative cooling, so that the classic *global* cooling flow catastrophe does not occur.

4.4. Changing Galaxy Optical Luminosity and Central Velocity Dispersion

All models presented in the previous Sections are characterized by the same optical luminosity and central velocity dispersion. How does the gas flow evolve in galaxies with different optical luminosity and central velocity dispersion? In particular, is the evolution of models characterized by $\vartheta_{\rm SN} = 2/3$ peculiar to high SNIa rate models or is the WOI scenario still valid if we reduce the present day SNIa rate to the current (optically) estimated $\vartheta_{\rm SN} = 1/4$ (and rescaling accordingly the amount and/or distribution of the dark matter content)? We present here few selected models of an extensive work (in progress) aimed at investigating the properties of a large set of galaxy models. In all of the following models $s = 1.6$ in order to match the observed iron in the ICM (see Renzini et al. 1993). As already anticipated by CDPR, the main result is an extreme sensitiveness to the value of the central velocity dispersion. For example, model #18 ($L_{\rm B} = 3 \times 10^{10} L_\odot$, $\sigma_{\circ *} = 200$ km s^{-1}) remains in the *wind* phase over all its evolution. Model #19 has the same parameters as model #18, but a slightly higher central velocity dispersion (i.e., a slightly deeper potential well), $\sigma_{\circ *} = 210$ km s^{-1}. In this case $t_{\rm cc} \simeq 9.5$ Gyrs, while in model #20 ($\sigma_{\circ *} = 220$ km s^{-1}), $t_{\rm cc} \simeq 4.6$ Gyrs. In model #21 ($L_{\rm B} = 4 \times 10^{10} L_\odot$, $\sigma_{\circ *} = 210$ km s^{-1}) $t_{\rm cc} \simeq 9.6$ Gyrs, while in the model #22 ($\sigma_{\circ *} = 220$ km s^{-1}) $t_{\rm cc} \simeq 7.2$ Gyrs. The evolution of these models is very similar to that of the models presented in the previous Sections: for example, in Fig.9 (upper panel) the evolution of the X–ray luminosity of model #21 is shown, and the similarity with that of models #1,2,3 is apparent. Also the duty cycles span the same range of values: $f_{\rm BH} = (4.7,\ 5.6,\ 1.7,\ 2.7) \times 10^{-4}$ in models #(19, 20, 21, 22)

Of course, due to the dependence of the stellar mass loss on the parent galaxy optical luminosity, the accreted mass in the galaxy center is correspondingly reduced, with $\Delta M_{\rm BH} \simeq (0,\ 6.5 \times 10^7,\ 2.9 \times 10^8) M_\odot$ in models #(18,19,20), and $\Delta M_{\rm BH} \simeq (4.8 \times 10^7,\ 1.2 \times 10^8) M_\odot$ in models #(21,22). Note the dependence of $\Delta M_{\rm BH}$ on $\sigma_{\circ *}$ (see Section 5).

In all the models presented above $T_{\rm X} = 10^9$ K, $\epsilon = 0.1$, and $\mathcal{R} = 2$. A reduction of $T_{\rm X}$ obviously increases the mass accreted in the center, but does not alter dramatically the evolution (as far as its value is higher than the mean gas temperature, the basic assumption of this paper): for example, in model #21r (Fig.9, lower panel) we assumed $T_{\rm X} = 2 \times 10^8$ and we obtained

$\Delta M_{\rm BH} \simeq 1.4 \times 10^8$ and $f_{\rm BH} = 6.2 \times 10^{-4}$. Relevant overall properties of these models are displayed in Table 3.

5. Discussion and Conclusions

In this paper we have investigated the behavior of the galactic gas flows in early type galaxies, assuming at their center the presence of a massive BH growing with the accretion of matter and affecting the inflow through feedback. The interaction of the radiation produced by accretion with the hot, X–ray emitting gas of the halo has been studied, considering the effects of Compton heating and cooling, bremsstrahlung recycling, variable ionization state in the cooling function and hydrogen and helium photoionization heating. The basic assumption of these models is that the Compton temperature of the radiation emitted by the accreting material is substantially higher than the mean gas temperature of the galactic ISM, consistent with the finding that nearby AGN in elliptical galaxies have $T_{\rm X} \simeq 5 \times 10^8$ K.

The characteristics of the flow and of the resulting luminosity are studied by changing the efficiency of conversion of the accreted mass into radiation, the Compton temperature of the emitted radiation, the rate of SNIa explosions and the amount of dark matter. A qualitative exploration is also performed in order to understand the effect of the presence of a physically thin, optically thick accretion disk, where the inflowing gas is stored before being released with a characteristic time scale on the BH and radiation is emitted only in a cone, or alternatively an ADAF solution, characterized by accretion–dependent low luminosity.

The resulting evolution of the flow – and consequently of the emitted luminosities, both coronal ($L_{\rm X}$) and central ($L_{\rm BH}$) – is sensitive to all these parameters, but *the gas flows are found invariably unstable to Compton heating.* Before discussing the variants let us note the properties in common to all of the models:

- At late epochs (comparable to the current Hubble time), all models show a type of relaxation oscillation. They spend a small fraction of the time ($10^{-2} - 10^{-4}$) in an AGN state of high BH luminosity ($10^{45} - 10^{47}$ erg s^{-1}), and the bulk of the time with the AGN "turned off" and the ambient gas emitting X–rays in what would appear to be a proto–cooling phase state.

- Mass dropout and accreted mass are small compared to naive estimates based on gas mass/cooling time because the time averaged heat input from the central BH balances the gas radiative cooling.

- The central BH grows by episodic accretion up to a mass in the observed range ($10^{8.5} - 10^{9.5} M_{\odot}$) in all giant ellipticals, even though only $\approx 10^{-3}$ of them will be observed in an AGN phase.

- Due to the self regulating nature of the feedback, all the computed observables are relatively insensitive to the assumed efficiency (in the range investigated).

For all the computed models, of which only a small but representative sample is described in this paper, the gas opacity to $L_{\rm BH}$ remains very small in all evolutionary phases, as predicted by BT95 and by our introductory analysis: the fraction of the emitted luminosity effectively absorbed by the halo gas is of the order of $10^{-4} - 10^{-3}$, and never larger than 10^{-2}. Moreover, the effect of photoionization heating is found to be negligible, due to the high temperatures reached by the gas during the central bursts.

For high efficiency values ($\epsilon \simeq 0.1$), the flow evolves through strong oscillatory phases: short bursts of accretion that last few Myrs, with a rich temporal sub–structure, and in which the radiation emitted by the central source overcomes the luminosity emitted by the coronal gas, are followed by longer periods (of the order of Gyrs) in which the BH is quiescent, and the X–ray luminosity is due only to the coronal gas. The quiescent phases are a consequence of the galaxy degassing following the strongest central accretion events, when a substantial fraction of the galaxy hot gas is lost. We note that the high metallicity seen in the ICM of typical rich clusters provides strong observational evidence for significant wind and outgassing phases. The decreased gas density reduces dramatically the radiative losses, and the inflow stops. After the time required for the stellar mass loss to replenish the galaxy and so to restore the radiative losses, a new global cooling catastrophe takes place, the BH re–ignites, and a cycle restarts. The maximum luminosities reached during the accretion events can be of the order of $10^{47} - 10^{48}$ erg s^{-1}, but the duration of the single accretion events are extremely short. Correspondingly, the accretion rates can reach values as high as $10^2 M_{\odot}$ yr^{-1}, but the total mass accreted by the BH at the end of the simulation is a few $10^8 M_{\odot}$, very low compared to the amount that the galaxy expels during the BH bursts. $L_{\rm X}$ is strongly correlated with the amount of hot gas inside the galaxy, and so after a degassing event the galaxy X–ray luminosity can drop by a factor of 100 or more, and successively increase together with the gas amount inside the galaxy. The luminosity of the central AGN and the ambient gas are strongly anticorrelated.

Reducing the efficiency, the time elapsed in the phases of BH activity becomes longer and longer, and for very low efficiency values the global degassing events completely disappear, leaving a continuous flickering of $L_{\rm BH}$. The values of $L_{\rm BH}$ in these circumstances are still high, $\sim 10^{46}$ erg s^{-1} at peaks, and the final mass of the BH is much higher than in case of high efficiency, reaching values as high as $10^9 M_{\odot}$ or more.

Models in which the SNIa rate was decreased or the dark matter halo mass was increased, and so $t_{\rm cc}$ is anticipated at early times, have been successively investigated. The differences between high and low efficiency accretion hold also for this class of models, and are essentially the same as for late times cooling catastrophe. The only quantitative differences concern the time elapsed between two successive global degassing events. In this case the time is shorter, consistently with the faster time evolution of the mass return from the stellar galactic population at early times.

For these models the central BH grows to over $10^{11} M_{\odot}$ in case of no feedback. However, it was shown that the epoch of the cooling catastrophe is extremely sensitive to the value of the model central velocity dispersion, and that even galaxies with a SNIa rate consistent with the current optical estimates and of considerable optical luminosity ($L_{\rm B} \geq 3 \times 10^{10} L_{\odot}$) can easily develop a *late* cooling catastrophe and successive global degassing events.

Two more classes of models were explored in semi–quantitative fashion, in order to explore the main effects of non–spherically symmetric accretion. In the first class, we studied the effects of the presence of a physically thin, but optically thick accretion disk around the BH, where the infalling gas is stored and successively released with some time scale. The same disk funnels most of the radiation into a polar cone from which only the Thomson back–scattered component is able to Compton heat the gas. Now, with the overall efficiency reduced by a factor $\tau \sim 10^{-2} - 10^{-1}$, the solution is similar to that of low efficiency models. In these models, the major degassing events are suppressed, and only a (strong) flaring activity persists. The central BH can accrete up to nearly $10^{10} M_{\odot}$ over the Hubble time. More interesting is the case of a central ADAF. In fact, at variance with simple expectations, the accretion–dependent efficiency characterizing these solutions produces an efficient galaxy degassing.

As an important point, we point out here that all the simulations confirm the simple energetic expectations worked out in the Introduction, i.e, the fact that the energetic balance in our model is critical: in fact, we found both models with global degassing and models presenting only strong instabilities in the accretion, but without major degassing events.

A delicate issue which applies to all computed models concerns the temporal structure of the sub–bursts. We sampled $L_{\rm BH}$ and $L_{\rm X}$ at very high temporal resolution, and we found that each sub–burst is temporally extended for several time–steps. This fact is interesting for two reasons: the first is that the sub–bursts are not numerical artifacts, produced by the time–discretization used by the numerical scheme of integration, but real phenomena of the models. The second fact is that each sub–burst extends temporally approximately over the free–fall time from the first active grid–point (Section 3.1). So, not only is this phenomenon well described numerically, but also *physically*, at least consistently with the adopted spatial discretization. Obviously, by reducing the grid spacing in the inner regions the temporal resolution can be increased. We performed many simulations with a reduced grid spacing, and the final result was that we obtained a better temporal resolution of each burst, finding that each is subdivided into an increasing number of shorter sub–bursts. At the same time, the total time of each burst, the accreated mass, the emitted luminosity are in good agreement with those derived using the standard grid, and so we believe we have captured the physics of the phenomenon. In any case, it is clear that only using a grid with extremely high spatial resolution, that samples the flow well inside $R_{\rm X}$, can the substructure of a burst be studied in full detail. This kind of simulation, with several grid points inside $R_{\rm X}$ and the outermost one placed at few pc, will be presented in a later work. It represents the complementary exploration to that performed in this paper, allowing a comparison with observations of AGN variability.

How can our results be interpreted in the more global context of the X–ray luminosity evolution of the bulk of elliptical galaxies? In the modeling of gas flows *without* a central engine, two different possibilities have been explored in the past: in the first the SNIa heating is so low that the galaxies are not able to expel their coronal gas, and so all galaxies should host an inflow. The three main problems encountered by this scenario are that the expected X–ray luminosity is substantially higher than that observed, the related difficulty in explaining the observed scatter of $L_{\rm X}$ at fixed optical luminosity, and finally the disposal of the gas that cools and accumulates in the galaxy centre in a standard cooling flow.

These problems could be partially solved in the WOI scenario, in which a time decreasing SNIa rate is sufficient to sustain a wind. In this class of models the observed scatter in the $L_{\rm B}$–$L_{\rm X}$ plane is a direct consequence of the deepening of the galactic potential well with increasing $L_{\rm B}$, as dictated by the Fundamental Plane. This scenario solves also the problem of the mass accreted in the galaxy center over an Hubble time by cooling flow galaxies, being the major fraction of the gas lost by the stars ejected from the galaxies in their early wind phase, when also the mass return is higher. However, as discussed in the Introduction, objections have been raised on the validity of this scenario, on the ground of the apparent lack of detection of a sufficient amount of iron in the ISM of some ellipticals. Obviously, for a null SNIa rate, the WOI scenario does not apply, and the cooling flow solution, together with its unsolved problems, would remain the only workable model. In any case, even with enhanced supernova activity up to the current optical estimates, the cooling catastrophe is only delayed, not avoided, so the mass disposal problem remains for massive galaxies.

Following the observational consequences that can be derived from the class of models presented in this paper, a solution to the previous problems can be obtained quite easily, mainly due to the strong and temporally discontinuous variability of $L_{\rm BH}(t)$ and $L_{\rm X}(t)$.

The first observational consequence of our models is that the duty cycle of the central engine, even in models unable to produce substantial global degassing events, is very low, never exceeding 10^{-1} and typically of order 10^{-2} to 10^{-3}. For high efficiency accretions this quantity can be as low as 10^{-4}, and its value increases for low efficiency. The details for each model are given in Table 1. These numbers are small, and could be an alternative explanation to that advocated by Fabian & Rees (1995) in order to explain why the nuclei of elliptical galaxies are normally not luminous sources as a result of the accretion of the hot gas by the central BH.

A second interesting aspect of the presented models is that the total mass accreted on the galactic center over an Hubble time, even in the case of an early cooling catastrophe, is low compared to the same quantity for a pure cooling flow solution (or even for inflow solution in the CDPR models, see Table 1). We note that the accreted masses are comparable (with the exceptions of models #0 and 15), to the masses observed in massive central black holes, so the *feedback modulated accretion flows* could provide a natural way to grow black holes to the observed masses (see, e.g., Kormendy & Ho 2000).

Recently it has been determined that $M_{\rm BH}$ correlates extremely well with $\sigma_{\circ *}$, with $M_{\rm BH} \propto \sigma_{\circ *}^{4\div 5}$ (see, e.g., Ferrarese & Merritt 2000, Gebhardt et al. 2000): we note here that $\Delta M_{\rm BH}$ in galactic models differing only in the value of their central velocity dispersion (models #19,20 and #21,22 in Section 4.4) also increases with $\sigma_{\circ *}$. Of course, the scatter of $\Delta M_{\rm BH}$ of models in Table 1 is larger than that observed: a reduced scatter would be predicted if (for example) the accretion efficiency and the present SNIa rate were fixed numbers.

A third aspect to be mentioned is the evolution of the hot gas X–ray surface brightness profiles: in fact one of the many problems of the cooling flow models is that the resulting X–ray profiles $\Sigma_{\rm X}(R)$ are cuspy, at variance with the observations (Sarazin & Ashe 1989). As already pointed out by BT95 and CO97, in this new class of solutions characterized by feedback from the galactic central regions, the profiles have a well defined core, as in the case of the outflow solution of CDPR, except during the central burst phases, when the $\Sigma_{\rm X}$ shape presents many features. In Fig.10 we show the surface brightness profiles of a model representative of the case in which global degassing events take place (model #1, upper panel), and of a model presenting only strong temporal variations of the accretion (model #7, lower panel). The profiles are sampled at ten different times, equally spaced of 0.5 Gyr, starting from 9.5 Gyr (after the cooling catastrophe of model #1). The heavy lines in both panels are the X–ray surface brightness profile of the corresponding models without the central BH, at a representative time (12 Gyr). The profiles are obtained using a projection routine based on the Raymond–Smith thin plasma code (Raymond & Smith 1977). The absence of the central cusp in these models is apparent, except for the very cuspy profile in the lower panel, representing a model caught during an accretion event.

The total time in which $\Sigma_{\rm X}$ of model #1 is significantly disturbed is much less than 10 per cent of the time after the cooling catastrope (~ 6 Gyr), considerably more in model #7. Thus the duty cycle of Compton perturbations in $\Sigma_{\rm X}$ is much greater than that of the central $L_{\rm BH}$.

The presence of these large–scale features is clearly an important observational test for the scenario explored in this paper. Certainly models such as #7 (e.g., #8,9,10,11,12, lower panel in Fig. 10) are characterized by very noisy $\Sigma_{\rm X}$ profiles, and so observations probably are already in conflict with them. On the contrary, the profiles of models similar to #1 (e.g., #2,3,4,5,6,13,21,1r,2r,21r and others, upper panel in Fig. 10) are considerably smoother, essentially over all the galaxy lifetime. For these latter models the only significant feature in the $\Sigma_{\rm X}$ profile is the short–lived, X–ray bright shell visible in the higher profile in Fig. 10 (upper panel). The observational properties of this feature have been described in CO97.

A fourth important point is the aid these models can give to the solution of the observed scatter in the $L_{\rm B}$–$L_{\rm X}$ plane, as preliminarily discussed in CO97. In fact, in our models $L_{\rm X}$ shows large variations in its intensity (see, e.g., Fig.2, and Table 1). However, the definitive answer to the problem of the $L_{\rm B}$–$L_{\rm X}$ scatter could be more complicated. In fact, recent observational findings (Mathews & Brighenti 1998, Fukugita & Peebles 1999), albeit based on just 11 galaxies and all of relatively high X–ray luminosity, seem to show a correlation $L_{\rm X} \propto R_{\rm Xe}^{\alpha}$, where $R_{\rm Xe}$ is the X–ray

effective radius and α is a positive number ($\alpha = 0.6 \pm 0.3$ in Mathews & Brighenti 1998). As well known, this is at odds with the predictions of cooling flows and CDPR inflow models: only during CDPR *outflowing* models this correlation could be established. Also the X–ray luminosity of the models here presented is (statistically) anticorrelated with $R_{\rm Xe}$, as can be clearly seen in the upper panel of Fig.10, where the lower profiles (i.e., low $L_{\rm X}$) are also the more extended (i.e., large $R_{\rm Xe}$). A possible explanation for $L_{\rm X} - R_{\rm Xe}$ relation could involve environmental effects, as proposed by Mathews & Brighenti.

Summarizing, if the WOI scenario applies, small galaxies do not experience in their life any cooling catastrophe, and their luminosity evolution would be the same as described in CDPR, with low $L_{\rm X}$ and no significant nuclear activity. The nuclear activity should predominate in medium-high luminosity galaxies, but the probability of catching a peak of $L_{\rm BH}$ is small, of the order of a few per cent or less, as obtained from the performed numerical simulations with high efficiency; a larger fraction of the galaxies *hosting a BH at their center* should be caught in a nuclear outburst if the efficiency of the accretion is low. Note that, if the origin of the QSO phenomenon is associated with the initial cooling catastrophe, then we have a model for the "clock": for example, in a standard ΛCDM universe ($h = 0.65$, $\Omega_{\rm m} = 0.3$, $\Omega_\Lambda = 0.7$, see, e.g., Bahcall et al. 1999) $t_{\rm cc} = (4, 7, 9)$ Gyr corresponds to $z = (1.7, 0.8, 0.5)$.

Certainly the presented models have some weaknesses: first of all the assumption of spherical symmetry overall, but we think that the present investigation is sufficiently promising that a more demanding effort is justified. In the real accretion phenomena non axisymmetric effects in the infalling gas are very likely to occur outside of the central regions. Also, outflows may occur in the polar directions (cfr. BT95 and Park & Ostriker 1999) as jets, thus changing the total amount of accreted mass with respect to the spherically symmetric estimates here presented. The interaction between these jets and the hot gaseous halo can be investigated only with a 2D code. Another important question that requires (at least) a 2D treatment is the possibility of instabilities in the gas flow. Particularly, from our simulations it appears that a transient cold shell of material surrounds a hot central bubble during the flaring activity, especially in the case of low efficiency. This would evolve into a Rayleigh–Taylor instability for the shell, that certainly will break, permitting cold fingers of material to accrete on the BH. It is then clear that a fully 2D hydrodynamical analysis is required for a better understanding of this accretion problem. The unstable nature of the gas flows in elliptical (without central BHs) has been found by 2D numerical simulations, (D'Ercole & Ciotti 1998, D'Ercole, Recchi, & Ciotti 1999), especially when a substantial SNIa rate (even though not sufficient to extract the gas from the galaxy potential well) is present. In these cases, transient cold filaments form and are accreted on the center: in case of presence of a BH the situation should evolve in a very complex way.

Another potential problem of the presented scenario is the value of the temperature of the radiation emitted during the accretion events. While the adopted value is higher than the mean gas temperature of the ISM it is obvious that, in case of considerably lower radiation temperature *Compton cooling* is expected, with a stronger tendency towards a *radiation induced cooling flow*,

as stated by Nulsen & Fabian (1999) (see Section 4.2.4). As a consequence, one should observe an even *higher* luminosity from the centers of elliptical galaxies (although at low temperatures) than that predicted by the simple energetic argument presented in the Introduction. A possible solution to this problem could be a significant mass dropout from the cooling flow, well outside the galaxy center. For values of T_X moderately smaller than assumed in the bulk of models presented in this paper (but larger than T_{gas}) one can, without further computations, find the approximate solution by scaling T_X down and ϵ up by the same factor.

As a final comment on the present models, it seems to us unescapable that in every case the presence of a massive BH at the center of elliptical galaxies must produce a very strong feedback on the flow itself, either of energetic nature, mainly via Compton heating (or cooling, depending on the range of T_X, as discussed in this paper), or via mechanical heating, as discussed in BT95. It is important to stress that both investigations, that given by BT95 and that presented in CO97 and in this paper, are not in opposition to one another, but complementary, demonstrating that in the presence of a massive BH the possibility of a stationary cooling flow seems to be very remote; it is instead more likely that a global equilibrium will be achieved wherein the time–averaged heating and cooling rates are approximately in balance.

Finally, we can speculate on the physical status of the gas in rich galaxy clusters, assuming the presence of a massive BH at the center of the cD galaxy. In this case a global degassing cannot be expected, but the effect of the radiation feedback on the ICM should be still strong, and the standard cooling flow scenario modified accordingly. We point out that observations are available supporting the scenario here presented, for example strong evidence of intermittent cooling flows at the center of galaxy clusters (see, e.g., McNamara 1999, Soker et al. 2000), and the failure of detection of the expected amount of cold gas in the center of clusters (Miller, Bregman & Knezek 1999). And finally there is considerable evidence (see, e.g., Suginohara & Ostriker 1998, Pen 1999, and references therein) for additional source of entropy in the central regions of clusters.

We would like to thank James Binney, Piero Madau and Bohdan Paczynski for useful discussions and advice, and Thierry Courvoisier for providing us the spectral energy distribution of 3C 273. L.C. wishes also to thank Giuseppe Bertin, Fabrizio Brighenti, Alberto Cappi, Gabriele Ghisellini, Silvia Pellegrini, Alvio Renzini and Gianni Zamorani for useful discussions. A particular acknowledgement is due to Annibale D'Ercole for his advice on the original hydrodynamical code. The anonymous referees are thanked for useful comments that improved the presentation of the paper. L.C. was supported by NSF Grant AST9108103, by ASI, contract ASI-95-RS-152, and by MURST, contract CoFin98. J.P. Ostriker was supported by NSF grant # 94-24416.

A. The Input Physics

We describe here the main ingredients entering the heating and cooling terms $L_{\rm h}$ and $L_{\rm r}$ in the hydrodynamical equations (14)-(16).

A.1. Compton Heating and Cooling

Under the assumption of spherical symmetry, the gas Compton heating (or cooling) for unit frequence at radius r is given by:

$$\Delta E_{\rm C} = -N_{\rm scatt}(\nu, r)\Delta E_{\gamma}(\nu, T), \tag{A1}$$

where $\Delta E_{\rm C}$ is the gas energy for unit volume gained (or lost) by the gas at the frequence ν and at the radius r, and ΔE_{γ} is the energy variation of a photon of frequency ν interacting with an electron at the gas temperature $T(r)$. The number of photon-electron scatterings can be written as:

$$N_{\rm scatt}(\nu, r) = N_{\gamma}(\nu, r) \times \frac{\sigma_{\rm KN}(\nu) n_{\rm e}(r)}{4\pi r^2} = \frac{L_{\rm BH}(\nu, r)\Delta t}{h\nu} \times \frac{\sigma_{\rm KN}(\nu) n_{\rm e}(r)}{4\pi r^2}, \tag{A2}$$

where $n_{\rm e}(r)$ is the electron number density, $L_{\rm BH}(\nu, r)$ is the BH luminosity at the radius r, and $\sigma_{\rm KN}(\nu) = \sigma_{\rm T}\tilde{\sigma}_{\rm KN}(x)$ is the Klein–Nishina cross–section. $\sigma_{\rm T} \simeq 6.65 \times 10^{-25}$ cm^2 is the Thomson cross section, $x = \nu h / m_{\rm e}c^2$, and

$$\tilde{\sigma}_{\rm KN}(x) = \frac{3}{4}\left\{\frac{1+x}{x^2}\left[\frac{2(1+x)}{1+2x} - \frac{\ln(1+2x)}{x}\right] + \frac{\ln(1+2x)}{2x} - \frac{1+3x}{(1+2x)^2}\right\} \tag{A3}$$

(Lang 1980, p.68). A simple approximation for the energy transfer factor is[4]:

$$\Delta E_{\gamma}(\nu, T) = \frac{4k_{\rm B}Tx(1+3x^2/8)}{1+x^3} - \frac{m_{\rm e}c^2x^2(1+x^2)}{1+x^3}. \tag{A4}$$

After substitution of equations (A2) and (A4) in equation (A1) one obtains

$$\left(\frac{\partial E}{\partial t}\right)_{\rm C} = -E\frac{8}{3}\frac{n_{\rm e}(r)}{n_{\rm T}(r)}\frac{L_{\rm BH}(\nu, r)}{m_{\rm e}c^2}\frac{\sigma_{\rm KN}(x)}{4\pi r^2}\Delta(x, T), \tag{A5}$$

where $\Delta(x, T) \equiv \Delta E_{\gamma}(\nu, r)/4k_{\rm B}Tx$. Note that $L_{\rm BH}(\nu, r)$ satisfy the continuity equation

$$\frac{\partial L_{\rm BH}(\nu, r)}{\partial r} = -4\pi r^2 \left(\frac{\partial E}{\partial t}\right)_{\rm C}. \tag{A6}$$

---

[4] This formula reproduces the well known relations $\Delta E_{\gamma} \sim 1.5k_{\rm B}T - m_{\rm e}c^2x + O(1/x)$ for relativistic photon energy ($h\nu \gg m_{\rm e}c^2$), and $\Delta E_{\gamma} \sim 4k_{\rm B}Tx - m_{\rm e}c^2x^2 + O(x^3)$ in the classical limit.

We speed up the numerical simulations assuming a *gray* absorption, i.e., at any radius $L_{\rm BH}(\nu, r) = f_\circ(\nu) L_{\rm BH}(r)$. With this choice, and after integration of equation (A5) over all frequencies, one has:

$$\left(\frac{\partial E}{\partial t}\right)_{\rm C} = -E \frac{8}{3} \frac{n_{\rm e}(r)}{n_{\rm T}(r)} \frac{\sigma_{\rm T}}{4\pi r^2} \frac{L_{\rm BH}(r)}{m_{\rm e} c^2} C_{\rm X} \left[1 - \frac{T_{\rm X}}{T(r)}\right], \tag{A7}$$

where

$$C_{\rm X} = \int_0^\infty \frac{(1+3x^2/8)\tilde{f}_\circ(x)\tilde{\sigma}_{\rm KN}(x)}{1+x^3}\, dx = 0.137, \tag{A8}$$

and the spectral temperature is given by:

$$T_{\rm X} = \frac{m_{\rm e} c^2}{4 k_{\rm B} C_{\rm X}} \int_0^\infty \frac{x(1+x^2)\tilde{f}_\circ(x)\tilde{\sigma}_{\rm KN}(x)\, dx}{1+x^3} = 1.04 \times 10^9 \quad {\rm K}. \tag{A9}$$

The two numerical values are obtained using $f_\circ$ as given by equation (10). The radial dependence of $L_{\rm BH}$ is now obtained by integrating equation (A6) over all the frequencies, by using equation (A7), and finally integrating the resulting differential equation:

$$L_{\rm BH}(r) = L_{\rm BH}(0) \exp\left[\frac{8}{3} \frac{\sigma_{\rm T} C_{\rm X}}{m_{\rm e} c^2} \int_0^r E \frac{n_{\rm e}}{n_{\rm T}} \left(1 - \frac{T_{\rm X}}{T}\right) dr\right]. \tag{A10}$$

$L_{\rm BH}(0)$ is the bolometric luminosity emitted by the accreting material on the central BH, as given by equation (1). Equation (A7) can now be integrated with respect to time.

A.2. Photoionization Heating

We consider three photoionization processes, one for the hydrogen and two for the helium. For each of the processes an equation similar to equation (A1) holds:

$$\Delta E_{\rm ph} = -N_{\rm ph}(\nu > \nu_{\rm i}, r) \Delta E_\gamma(\nu, \nu_{\rm i}), \tag{A11}$$

where $\nu_{\rm i}$ is the ionization frequency of HI, HeI and HeII. Moreover,

$$N_{\rm ph}(\nu > \nu_{\rm i}, r) = N_\gamma(\nu > \nu_{\rm i}, r) \times \frac{\sigma_{\rm i}(\nu) n_{\rm i}(r)}{4\pi r^2} = \frac{L_{\rm BH}(\nu > \nu_{\rm i}, r)\Delta t}{h\nu} \times \frac{\sigma_{\rm i}(\nu) n_{\rm i}(r)}{4\pi r^2}, \tag{A12}$$

where the ionization energies are $(h\nu_{\rm HI}, h\nu_{\rm HeI}, h\nu_{\rm HeII}) = (13.598, 24.587, 54.416)$ eV (Lang 1980, p.246), $\sigma_{\rm i}(\nu) = \sigma_{\rm i\circ}\tilde{\sigma}_{\rm i}(\nu/\nu_{\rm i})$ are the photoionization cross–sections, and $n_{\rm i}(r)$ is the number (per unit volume) of HI, HeI, and HeII atoms, respectively. For HI and HeII atoms in the non–relativistic regime,

$$\tilde{\sigma}_{\rm i}(y) = \frac{1}{y^4} \frac{\exp[-4 {\rm arctg}(\sqrt{y-1})/\sqrt{y-1}]}{1 - \exp(-2\pi/\sqrt{y-1})}, \tag{A13}$$

and for HeI

$$\tilde{\sigma}_{\rm i}(y) = 1.66 y^{-2.05} - 0.66 y^{-3.05}, \tag{A14}$$

with $(\sigma_{\circ\mathrm{HI}}, \sigma_{\circ\mathrm{HeI}}, \sigma_{\circ\mathrm{HeII}}) = (3.441 \times 10^{-16}, 7.83 \times 10^{-18}, 8.5992 \times 10^{-17})$ cm^{-2}, (Osterbrock 1974, p.15; Lang 1980, p.469). For the exchanged energies we use the simple approximation $\Delta E_\gamma = h\nu_\mathrm{i} - h\nu$, and by integrating equation (A11) over all the frequencies three constants are derived:

$$C_\mathrm{i} = \frac{\nu_\mathrm{i}}{\nu_\mathrm{T}} \int_1^\infty \tilde{f}_\circ \left(\frac{x\nu_\mathrm{i}}{\nu_\mathrm{T}}\right) \left(1 - \frac{1}{x}\right) \tilde{\sigma}_\mathrm{i}(x)\, dx, \tag{A15}$$

with $(C_\mathrm{HI}, C_\mathrm{HeI}, C_\mathrm{HeII}) = (1.55 \times 10^{-6}, 2.99 \times 10^{-4}, 3.09 \times 10^{-6})$. Summing the rates for the three processes we finally obtain:

$$\left(\frac{\partial E}{\partial t}\right)_\mathrm{ph} = \frac{L_\mathrm{BH}(r)}{4\pi r^2} \sum_{i=1}^{3} C_\mathrm{i} \sigma_{\mathrm{i}\circ} n_\mathrm{i}(r). \tag{A16}$$

A.3. Bremsstrahlung Recycling

The luminosity emitted per unit volume and per unit frequence over the solid angle by bremsstrahlung radiation from a gas at temperature $T(r)$ and atomic number Z_i, is given by

$$\dot{E}_\mathrm{Br}(\nu, r) = \frac{2^{11/2}(\pi/3)^{3/2} Z_\mathrm{i}^2 g_\mathrm{ff} q_\mathrm{e}^6}{m_\mathrm{e}^2 c^4} n_\mathrm{e} n_\mathrm{i} \left(\frac{m_\mathrm{e} c^2}{k_\mathrm{B} T}\right)^{1/2} \exp\left(-h\nu/k_\mathrm{B}T\right). \tag{A17}$$

The bolometric bremsstrahlung luminosity is then given by:

$$\dot{E}_\mathrm{Br}(r) = \frac{2^{11/2}(\pi/3)^{3/2} Z_\mathrm{i}^2 \overline{g} q_\mathrm{e}^6}{h m_\mathrm{e} c^2} n_\mathrm{e} n_\mathrm{i} \left(\frac{k_\mathrm{B} T}{m_\mathrm{e} c^2}\right)^{1/2}, \tag{A18}$$

(Lang 1980, pp.46-48). Thus, the (normalized) bremsstrahlung spectral distribution is:

$$\dot{E}_\mathrm{Br}(\nu, r) = f_\mathrm{Br}(\nu) \dot{E}_\mathrm{Br}(r), \quad f_\mathrm{Br}(\nu) = \frac{g_\mathrm{ff}}{\overline{g}} \frac{h}{k_\mathrm{B} T} \exp\left(-h\nu/k_\mathrm{B}T\right). \tag{A19}$$

The equation for the energy transfer from photons to electrons is obviously analogous to equation (A1), where now:

$$N_\mathrm{scatt}(r, \nu) = \frac{L_\mathrm{Br}(r, \nu)\Delta t}{h\nu} \times \frac{n_\mathrm{e}(r) \sigma_\mathrm{KN}(\nu)}{4\pi r^2}. \tag{A20}$$

The total luminosity emitted by bremsstrahlung inside the region of radius r is given by:

$$L_\mathrm{Br}(r, \nu) = 4\pi \int_0^r r'^2 \dot{E}_\mathrm{Br}(r', \nu)\, dr'. \tag{A21}$$

In order to speed up the computation we use also for the bremsstrahlung emission the approximation of gray atmosphere and $g_\mathrm{ff}/\overline{g} = 1$. In this case, after integration over the frequency, we obtain:

$$\left(\frac{\partial E}{\partial t}\right)_\mathrm{Br} = -E \frac{8}{3} \frac{n_\mathrm{e}}{n_\mathrm{T}} \frac{\sigma_\mathrm{T}}{4\pi r^2} 4\pi \int_0^r r'^2 \dot{E}_\mathrm{Br}(r') F(r', r, y)\, dr', \tag{A22}$$

where, using eqs. (A4)-(A19), and defining $t(r') \equiv k_\mathrm{B} T(r')/m_\mathrm{e} c^2$:

$$F(r', r) = \int_0^\infty \tilde{\sigma}_\mathrm{KN}[t(r')y] \exp\left(-y\right) \left[\frac{1 + 3t(r')^2 y^2/8}{1 + t(r')^3 y^3} - \frac{T(r')y}{4T(r)} \frac{1 + t(r')^2 y^2}{1 + t(r')^3 y^3}\right] dy. \tag{A23}$$

A.4. Effective Cooling Function

The radiative losses (i.e., the cooling rate per unit volume) are described by the function $L_{\mathrm{r}} = n_{\mathrm{e}} n_{\mathrm{p}} \Lambda(T, \Xi)$, where

$$\Lambda(T,\Xi) = \begin{cases} [\Lambda_\circ(T) - B_\circ(T)] \exp(-100\ \Xi)\ + B_\circ(T) & \text{for } T \leq 10^8 \text{ K} \\ B_\circ(T) & \text{for } T \geq 10^8 \text{ K.} \end{cases} \tag{A24}$$

The function $\Lambda_\circ(T)$ (erg cm^3 s^{-1}) is given for example by Mathews & Bregman (1978) (after correction of a wrong sign in their formula):

$$\Lambda_\circ(T) = \begin{cases} 5.3547 \times 10^{-27} T & \text{for } 10^4 K \leq T \leq 1.3 \times 10^5 \text{ K,} \\ 2.1786 \times 10^{-18} T^{-0.6826} + 2.7060 \times 10^{-47} T^{2.976} & \text{for } 1.3 \times 10^5 \leq T \leq 10^8 \text{ K;} \end{cases} \tag{A25}$$

when $T \geq 10^8$ K (the bremsstrahlung branch) $B_\circ(T) = \Lambda_\circ(10^8)\sqrt{T/10^8}$. The ionization parameter Ξ is introduced in order to describe the effects on the radiative losses by the hydrogen photoionization, and

$$\Xi(r) = \frac{n_\gamma(\nu \geq \nu_{\mathrm{HI}})}{n_{\mathrm{H}}}, \tag{A26}$$

where n_γ is the number density of photons with an energy greater than the hydrogen ionization energy. The parameter Ξ can be easily derived in case of gray atmosphere as

$$n_\gamma(\nu \geq \nu_{\mathrm{HI}}) = \int_{\nu_{\mathrm{HI}}}^{\infty} \frac{L_{\mathrm{BH}} f_\circ(\nu)}{4\pi r^2 ch\nu} d\nu = \frac{L_{\mathrm{BH}}(r)}{4\pi r^2 m_{\mathrm{e}} c^3} \int_{\nu_{\mathrm{HI}}/\nu_{\mathrm{T}}}^{\infty} \tilde{f}_\circ(x) \frac{dx}{x}, \tag{A27}$$

where the dimensionless integral equals 47.813 when using the spectral energy distribution given in equation (10).

A.5. The Effective Gravitational Field

Photons emitted by the BH interacts with the surrounding gas not only by exchanging energy but also exchanging momentum. This results in a modification of the effective gravity in the momentum equation (15):

$$g_{\mathrm{eff}}(r) = -\frac{GM(r)}{r^2} \left[1 - \frac{n_{\mathrm{e}}(r) \int_0^\infty \sigma_{\mathrm{KN}}(\nu) L_{\mathrm{BH}}(\nu, r)\, d\nu}{4\pi G \rho(r) M(r) c}\right]. \tag{A28}$$

Note that, by imposing the vanishing of the effective gravitational field and assuming $M(r) = M_{\mathrm{BH}}$, one obtains the classical expression for the Eddington luminosity:

$$L_{\mathrm{Edd}} = \frac{4\pi G c M_{\mathrm{BH}}}{\sigma_{\mathrm{T}} C_{\mathrm{Edd}}} \frac{\rho(r)}{n_{\mathrm{e}}(r)}, \tag{A29}$$

where for the frequency distribution (10) one obtains $C_{\mathrm{Edd}} = 0.214$.

B. Numerical evaluation of $L_{\rm BH}$ with $t_{\rm accr} > 0$

We describe here the numerical technique used to compute numerically $L_{\rm BH}$.

Let R_1 the nearest grid–point to the center, ρ_1 and v_1 the density and the velocity of gas at this point, and t_{i+1} the present value of the time. We use the following approximation for the emitted luminosity:

$$L_{\rm BH}(t_{i+1}) = \frac{\epsilon c^2}{t_{\rm accr}} \int_0^{t_{i+1}} \mathcal{F}_{\rm BH}(t') e^{-(t_{i+1}-t')/t_{\rm accr}}\, dt', \tag{B1}$$

where $\mathcal{F}_{\rm BH}(t') = -4\pi R_1^2 \rho_1 v_1$ if $v_1 < 0$ and 0 otherwise. In this way we qualitatively describe the smooth release of gas from the accretion disk to the BH. For example, for a stationary accretion with $\mathcal{F}_{\rm BH} = \mathcal{F}_{\rm BH}(0)$ one obtains $L_{\rm BH}(t) = \epsilon c^2 \mathcal{F}_{\rm BH}(0)[1 - \exp(-t/t_{\rm accr})]$, and for an impulsive accretion $\mathcal{F}_{\rm BH} = M_{\rm accr}\delta(t)$, $L_{\rm BH}(t) = \epsilon c^2 (M_{\rm accr}/t_{\rm accr}) \exp(-t/t_{\rm accr})$. It is easy to prove the following identity:

$$L_{\rm BH}(t_{i+1}) = L_{\rm BH}(t_i) e^{-(t_{i+1}-t_i)/t_{\rm accr}} + \frac{\epsilon c^2 e^{-t_{i+1}/t_{\rm accr}}}{t_{\rm accr}} \int_{t_i}^{t_{i+1}} \mathcal{F}_{\rm BH}(t') e^{-(t_{i+1}-t')/t_{\rm accr}}\, dt'. \tag{B2}$$

In the integration of the hydrodynamical equations, the integral over the time-step of equation (B2) is required. Changing order of integration on $\Delta E_{\rm BH} = \int_{t_{\rm i}}^{t_{\rm i+1}} L_{\rm BH}(t)\, dt$ one obtains:

$$\Delta E_{\rm BH} = t_{\rm accr}[L_{\rm BH}(t_i) - L_{\rm BH}(t_{i+1})] + \epsilon c^2 \int_{t_i}^{t_{i+1}} \mathcal{F}_{\rm BH}(t') e^{-(t_{i+1}-t')/t_{\rm accr}}\, dt'. \tag{B3}$$

During each time–step the function $\mathcal{F}_{\rm BH}$ is defined as the linear interpolation between the initial and final time: the integral in equation (B3) can be explicitly calculated, and the computer time required for its evaluation is negligible.

Table 1. Overall properties of the presented models.

Model #	ϵ	$\vartheta_{\rm SN}$	$\mathcal{R}$	$t_{\rm cc}$	ADAF	$\Delta M_{\rm BH}$	$f_{\rm BH}$
0	0	2/3	7.8	9.05	No	1.5×10^{10}	–
1	0.1	2/3	7.8	9.05	No	1.0×10^{8}	1.0×10^{-4}
2	0.01	2/3	7.8	9.05	No	3.1×10^{8}	2.7×10^{-4}
3	0.001	2/3	7.8	9.05	No	4.3×10^{8}	3.8×10^{-4}
4	0.1	2/3	10	4.24	No	5.8×10^{8}	2.1×10^{-4}
5	0.01	2/3	10	4.24	No	7.0×10^{8}	2.6×10^{-4}
6	0.001	2/3	10	4.24	No	6.9×10^{8}	2.5×10^{-4}
7	0.1	1/4	7.8	0.25	No	3.5×10^{9}	1.5×10^{-3}
8	0.01	1/4	7.8	0.25	No	4.9×10^{9}	1.8×10^{-3}
9	0.001	1/4	7.8	0.25	No	5.0×10^{9}	1.7×10^{-3}
10	0.1	1/4	3.0	0.25	No	2.7×10^{9}	1.4×10^{-3}
11	0.01	1/4	3.0	0.25	No	4.4×10^{9}	1.9×10^{-3}
12	0.001	1/4	3.0	0.25	No	4.6×10^{9}	2×10^{-3}
13	0.1	2/3	7.8	9.05	Yes	2.1×10^{8}	1.2×10^{-4}
14	0.01	2/3	7.8	9.05	Yes	4.4×10^{9}	1.3×10^{-3}
15	0.001	2/3	7.8	9.05	Yes	1.5×10^{10}	3.3×10^{-3}
16	0.1	2/3	7.8	9.05	No	1.6×10^{9}	5.3×10^{-2}
17	0.1	2/3	7.8	9.05	No	1.6×10^{9}	5.4×10^{-2}
1r	0.1	2/3	7.8	9.05	No	4.5×10^{8}	4.1×10^{-4}
2r	0.01	2/3	7.8	9.05	No	4.0×10^{8}	3.5×10^{-4}
1rr	0.1	2/3	7.8	9.05	No	5.9×10^{8}	5.3×10^{-4}

Note. — All models in the table have $L_{\rm B} = 5 \times 10^{10} L_{\odot}$, $\sigma_{\circ *} = 280$ km s^{-1}, $r_{c*} = 350$ pc, $r_{\rm t} = 63$ kpc. The amount of dark matter is a free parameter, but its scale–length is fixed to $r_{\rm ch} = 4.2 r_{c*}$. $\Delta M_{\rm BH}$ is the accreted mass by the central BH in solar units at the end of the simulation, when $t = 15$ Gyr. Models #16,17 simulate the presence of a geometrically thin, optically thick accretion disk.

Table 2. Time averaged X–ray luminosity.

Model #	ϵ	$T_{\rm X}$	ADAF	$< L_{\rm X} >$
0	0	–	No	100
1	0.1	10^9	No	7.6
2	0.01	10^9	No	13
3	0.001	10^9	No	15
13	0.1	10^9	Yes	5.7
14	0.01	10^9	Yes	25
15	0.001	10^9	Yes	30
16	0.1	10^9	No	30
17	0.1	10^9	No	30
1r	0.1	10^8	No	10.6
2r	0.01	10^8	No	13.5
1rr	0.1	5×10^7	No	15.3

Note. — Time averaged X–ray luminosity $< L_{\rm X} >$ (for $t > t_{\rm cc}$) in the energy range $0.5 - 4.5$ keV, in units of 10^{40} erg s^{-1}, for all models in Table 1 with the same structural parameteres.

Table 3. Overall properties of models presented in Section 4.4.

Model #	L_B	$\sigma_{\circ *}$	t_{cc}	T_X	f_{BH}	ΔM_{BH}	$< L_X >$
18	3	200	–	10^9	–	0	1.4
19	3	210	9.5	10^9	4.7×10^{-4}	6.5×10^7	0.07
20	3	220	4.6	10^9	5.6×10^{-4}	2.9×10^8	0.24
21	4	210	9.6	10^9	1.7×10^{-4}	4.8×10^7	0.08
22	4	220	7.2	10^9	2.7×10^{-4}	1.2×10^8	0.27
21r	4	210	9.6	2×10^8	6.2×10^{-4}	1.4×10^8	0.2

Note. — All models in the table have $\epsilon = 0.1$, $\mathcal{R} = 2$, and $\vartheta_{SN} = 1/4$. Galaxy optical luminosities are in units of $10^{10} L_\odot$, and central velocity dispersions in km s^{-1}. Time averaged X–ray luminosity $< L_X >$ (for $t > t_{cc}$, except for wind model #18), is in units of 10^{40} erg s^{-1}.

REFERENCES

Arimoto, N., Matsushita, K., Ishimaru, Y., Ohashi, T., & Renzini, A. 1997, ApJ, 477, 128

Awaki, H., Koyama, K., Kunieda, H., Takano, S., Tawara, Y., & Ohashi, T. 1991, ApJ, 366, 88

Awaki, H. et al. 1994, PASJ, 46, L65

Bahcall, N.A., Ostriker, J.P., Perlmutter, S., & Steinhardt, P.J. 1999, *Science*, 284, 1481

Bertin, G., & Toniazzo, T. 1995, ApJ, 451, 111

Binney, J., & Tabor, G. 1995, MNRAS, 276, 663 (BT95)

Brighenti, F., & Mathews, W.G. 1996, ApJ, 470, 747

Brighenti, F., & Mathews, W.G. 1999, preprint, (astro-ph/9910556)

Buote, D.A. 1999, MNRAS, 309, 685 MNRAS, 296, 977

Buote, D.A., & Fabian, A.C. 1998, MNRAS, 296, 977

Cappellaro, E., Turatto, M., Tsvetkov, D.Y., Bartunov, O.S., Pollas, C., Evans, R., & Hamuy, M. 1997, A&A, 322, 431

Canizares, C.R., Fabbiano, G., & Trinchieri, G. 1987, ApJ, 312, 503

Ciotti, L. 1993, Ph.D. Thesis, Astronomy Dept., University of Bologna, Italy

Ciotti, L., D'Ercole, A., Pellegrini, S., & Renzini, A., ApJ, 376, 380 (CDPR)

Ciotti, L., & Ostriker, J.P. 1997, ApJ, 487, L105 (CO97)

Cowie, L.L., Ostriker, J.P., & Stark, A.A. 1978, ApJ, 226, 1041

D'Ercole, A., & Ciotti, L. 1998, ApJ, 494, 535

D'Ercole, A., Recchi, S., & Ciotti, L. 1999, preprint, (astro-ph/9910142)

Eskridge, P.B., Fabbiano, G., & Kim, D.W. 1995, ApJS, 97, 141

Fabbiano, G. 1989, ARA&A, 27, 87

Fabian, A.C., Nulsen, P.E.J., & Canizares, C.R. 1984, Nature, 311, 733

Fabian, A.C., & Rees, M.J. 1995, MNRAS, 277, L55

Ferrarese, L., & Merritt, D. 2000, ApJ, 539, L9

Forman, W., Schwarz, J., Jones, C., Liller, W., & Fabian, A. 1979, ApJ, 234, L27

Forman, W., Jones, C., & Tucker, W. 1985, ApJ, 293, 102

Fukugita, M., & Peebles, P.J.E. 1999, preprint (astro-ph/9906036)

Gebhardt et al. 2000, ApJ, 539, 13

Giacconi et al. 2000, preprint, (astro-ph/0007240)

Harms, R.J., et al.. 1994, ApJ, 435, L35

Ikebe, Y., et al. 1992, ApJ, 384, L5

Kim, D.W., Fabbiano, G., Matsumoto, H., Koyama, K., & Trinchieri, G. 1996, ApJ, 468, 175

King, I. 1972, ApJ, 174, L123

Kormendy, J., & Ho, L.C. 2000, preprint, (astro-ph/0003268)

Lang, K.R. 1980, Astrophysical Formulae, Springer-Verlag, New York

Loewenstein, M., Mushotzky, R.F., Tamura, T., Ikebe, Y., Makishima, K., Matsushita, K., Awaki, H., & Serlemitsos, P.J. 1994, ApJ, 436, L75

Lu, Y., & Yu, Q. 1999, preprint, (astro-ph/9911289)

Macomb, D.J., et al. 1995, ApJ, 449, L99

Madau, P., & Efstathiou, G. 1999, ApJ, 517, L9

McNamara, B.R. 1999, preprint, (astro-ph/9911129)

McNaron-Brown, K., Johnson, C.D., Dermer, C.D., & Kurfess, J.D. 1997, ApJ, 474, L85

Magorrian, J., et al. 1998, AJ, 115, 2285

Maraschi, L., et al. 1994, ApJ, 435, L91

Mathews, W.G., & Bregman, J.N. 1978, ApJ, 224, 308

Mathews, W.G., & Brighenti, F. 1998, ApJ, 493, L9

Mathews, W.G., & Brighenti, F. 1999, ApJ, 526, 114

Matsumoto, H., Koyama, K., Awaki, H., Tsuru, T., Loewenstein, M., & Matsushita, K. 1997, ApJ, 482, 133

Miller, E.D., Bregman, J.L., & Knezek, P.M. 1999, preprint, (astro-ph/9911021)

Mushotzky, R.F. 1999, in The Hy Redshift Universe, ASP Conference Series, vol. 193, p.323, A.J. Bunker & W.J.M. van Breugel, eds.

Mushotzky, R.F., Loewenstein, M., Awaki, H., Makishima, K., Matsushita, K., & Matsumoto, H. 1994, ApJ, 436, L79

Mushotzky, R.F., Cowie, L.L., Barger, A.J., & Arnaud, K.A. 2000, Nature, 404, 459

Narayan, R., & Yi, I. 1995, ApJ, 452, 710 (NY95)

Nulsen, P.E.J., Stewart, G.C., & Fabian, A.C. 1984, MNRAS, 208, 185

Nulsen, P.E.J., & Fabian, A.C. 1999, preprint, (astro-ph/9908282)

Ohashi, T., et al. 1990, in Windows on Galaxies, eds. G. Fabbiano, J.A. Gallagher, & A. Renzini (Dordrecht: Kluwer), 243

Osterbrock, D.E. 1974, Astrophysics of Gaseous Nebulae, W.H. Freeman and Company, San Francisco

Ostriker, J.P., McCray, R., Weaver, R., & Yahil, A. 1976, ApJ, 208, L61

Park, M.-G., & Ostriker, J.P. 1998, Adv. Space Res., 22, p.951

Park, M.-G., & Ostriker, J.P. 1999, preprint, (astro-ph/9901243)

Pellegrini, S., & Ciotti, L. 1998, A&A, 333, 433

Pellegrini, S. 1999, preprint, (astro-ph/9909458)

Pen, U. 1999, ApJ, 510, L1

Quataert, E., & Narayan, R. 1999, preprint, (astro-ph/9908199)

Raymond, J., & Smith, B. 1977, ApJS 35, 419

Rees, M.J. 1984, ARA&A, 22, 471

Renzini, A., Ciotti, L., D'Ercole, A., & Pellegrini, S. 1993, ApJ, 419, 52

Richstone, D.O. 1998, in IAU Symp. 184, The Central Region of the Galaxy and Galaxies, ed. Y. Sofue, in press

Sarazin, C.L. & Ashe, G.A. 1989, ApJ, 345, 22

Sarazin, C.L. & White, R.E.III 1987, ApJ, 320, 32

Sarazin, C.L. & White, R.E.III 1988, ApJ, 331, 102

Serlemitsos, P.J., Loewenstein, M., Mushotzsky, R., Marshall, F., & Petre, R. 1993, ApJ, 413, 518

Shakura, N.I., & Sunyaev, R.A. 1973, A&A, 24, 337

Shapiro, S.L. 1973, ApJ, 180, 531

Soker, M.N., White, R.E.III, David, L.P., McNamara, B.R. 2000, preprint (astro-ph/0009173)

Suginohara, T., & Ostriker, J.P. 1998, ApJ, 507, 16

Tammann, G. 1982, Supernovae: A Survey of Current Research, ed. M. Rees and R. Stoneham, Dordrecht: Reidel, 371

Türler, M., Paltani, S., Courvoisier, T.J.-L., et al. 1999, A&AS, 134, 89

van Leer, B. 1977, J. Comp. Phys., 23, 276

van der Marel, R.P., de Zeeuw, P.T., Rix, H.-W., & Quinlan, G.D. 1997, Nature, 385, 610

Vedder, P.W., Trester, J.J., & Canizares, C.R. 1988, ApJ, 332, 725

White, R.E.III, & Sarazin, C.L. 1991, ApJ, 367, 476

This preprint was prepared with the AAS LaTeX macros v4.0.

Fig. 1.— The time evolution of mass and energy budget of model #1. Masses are given in solar masses, mass rates in solar masses per year, and luminosity in erg per second. In panel a, the mass of gas inside $r_{\rm t}$ ($M_{\rm gas}$, dotted line), and the mass accreted by the BH ($M_{\rm sink}$, solid line) are shown. In panel b the mass return rate from the stellar population ($\dot{M}_*$) is represented by the dotted line, the rate of mass loss at the truncation radius $r_{\rm t}$ ($\dot{M}_{\rm out}$) by the dashed line, and finally the BH accretion rate ($\dot{M}_{\rm BH}$) by the solid line. In panel c the short dashed and long dashed lines represent $L_{\rm SN}$ and $L_{\rm grav}$, respectively. The solid line represents $L_{\rm X}$, the observable X–ray gas emission calculated inside $r_{\rm t}$ and in the range 0.5–4.5 keV. $L_{\rm BH}$ is represented by the dotted line. In panel d we show the time evolution of the gas temperature (solid line, scale on the left axis) and density (dotted line, scale on the right axis) at 20 pc from the center.

Fig. 2.— Time evolution of $L_{\rm X}$ for model #1 (solid line) and for model #0 identical to model #1 (dotted line), but without the feedback from the central BH. The time–averaged luminosity of the two models #0,1 are respectively 10^{42} and 7.6×10^{40} erg s^{-1}.

Fig. 3.— Evolution of several quantities for model #1 in the time interval 9.04 – 9.8 Gyr. The time sampling of the plotted quantities is 10^4 yr. The linestyle and physical units are the same as in Fig.1. Note the rich temporal sub–structure of each accretion event; moreover, the opposite trend of the temperature (solid line) and density (dotted line) in the central regions of the flow is apparent in panel c. Peak luminosities, not shown, reach 10^{47} erg s^{-1}.

Fig. 4.— Evolution of the temperature, density, and velocity profiles (upper, middle, and lower panels, respectively), of model #1. In each panel the time sequence is: solid, dotted, short-dashed, long-dashed, dotted-dashed, and the (constant) time interval is 10 Myr. The solid lines in the three columns are the profiles at 9.01, 9.06, and 9.2 Gyrs, i.e., just before (column 1) and just after (column 2) $t_{\rm cc}$, while the time sequence in column 3 starts at 9.2 Gyrs, after a strong central burst (cfr. with Fig.3c). Note that the ordinate scales in the first and third temperature and density panels cover identical ranges, allowinwg a direct comparison of the various profiles.

Fig. 5.— The evolution of $L_{\rm BH}$ and $L_{\rm X}$ for models #1,2,3, from 9 Gyr ($\simeq t_{\rm cc}$) to 15 Gyr, sampled at time intervals of 1 Myr. The accretion efficiency in the three models is $\epsilon = (0.1, 0.01, 0.001)$, respectively. The various linetypes are the same as in Fig.1c.

Fig. 6.— The evolution of $L_{\rm BH}$ and $L_{\rm X}$ for models #4,5,6, from 4.2 ($\simeq t_{\rm cc}$) to 15 Gyr, sampled at time intervals of 1 Myr. The accretion efficiency in the three models is again $\epsilon = (0.1, 0.01, 0.001)$, respectively, but the dark matter halo is more massive (see Table 1). The various linetypes are the same as in Fig.1c.

Fig. 7.— The time evolution of $L_{\rm BH}$ and $L_{\rm X}$ for models #7,10,17, from 9 Gyr to 9.5 Gyr (upper, middle, and lower panels, respectively). All three model are characterized by $\epsilon = 0.1$, and the various linetypes corresponds to those described in Fig.1. In model #17, $t_{\rm accr} = 10^4 T_{\rm X}$.

Fig. 8.— The evolution of $L_{\rm BH}$ and $L_{\rm X}$ for the "ADAF" models #13,14,15, from 9 Gyr ($\simeq t_{\rm cc}$)

to 15 Gyr, sampled at time intervals of 1 Myr. The accretion efficiency in the three models is $\epsilon = (0.1, 0.01, 0.001)$, respectively. The various linetypes are the same as in Fig.1c.

Fig. 9.— The evolution of $L_{\rm BH}$ (dotted line) and $L_{\rm X}$ (solid line) of models #21 (upper panel), and #21r (lower panel), sampled at time intervals of 1 Myr.

Fig. 10.— The X–ray surface brightness profiles (in arbitrary units) of models #1 (upper panel) and model #7 (lower panel) at ten different times, sampled at time intervals of 0.5 Gyr, and starting from 9.5 Gyr. The heavy solid lines are the X–ray surface brightness profiles of the corresponding models without central BH, at arbitrary time $t = 12$ Gyr.

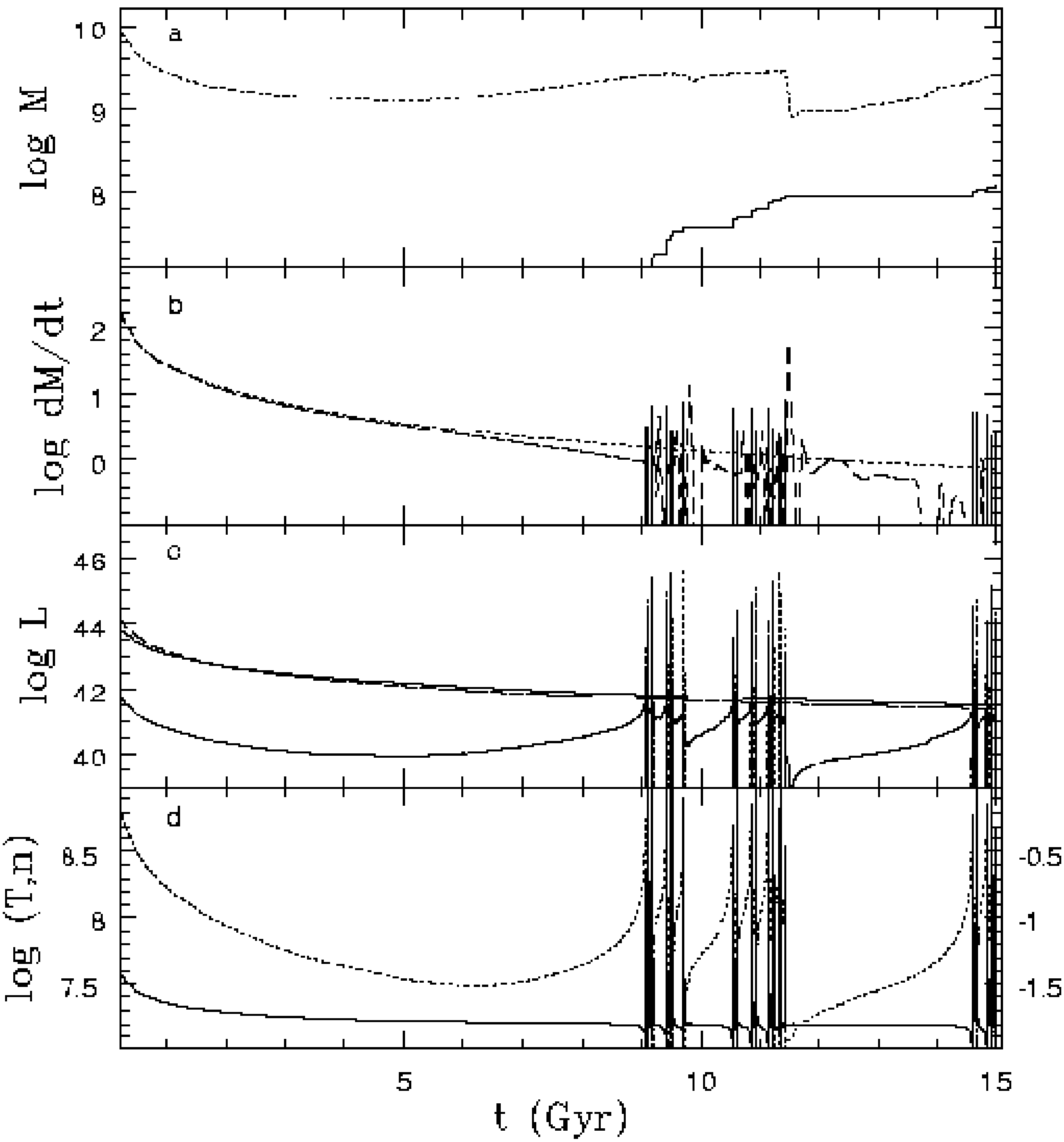
a
b
c
d
log M
log dM/dt
log L
log (T,n)
t (Gyr)
10
9
8
2
1
0
46
44
42
40
8.5
8
7.5
-0.5
-1
-1.5
5
10
15

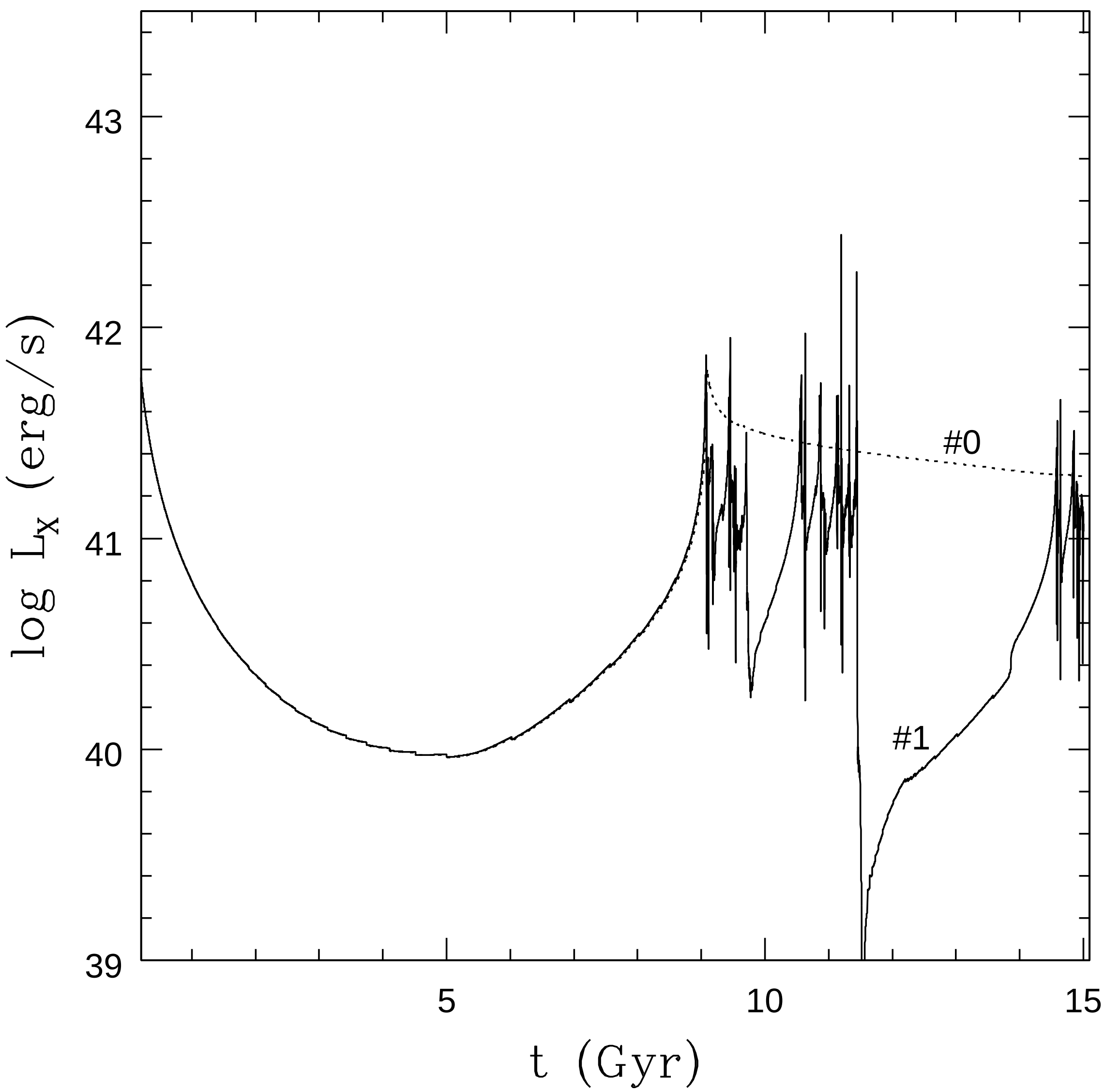

43
42
41
40
39
5
10
15
log L_X (erg/s)
t (Gyr)
#0
#1

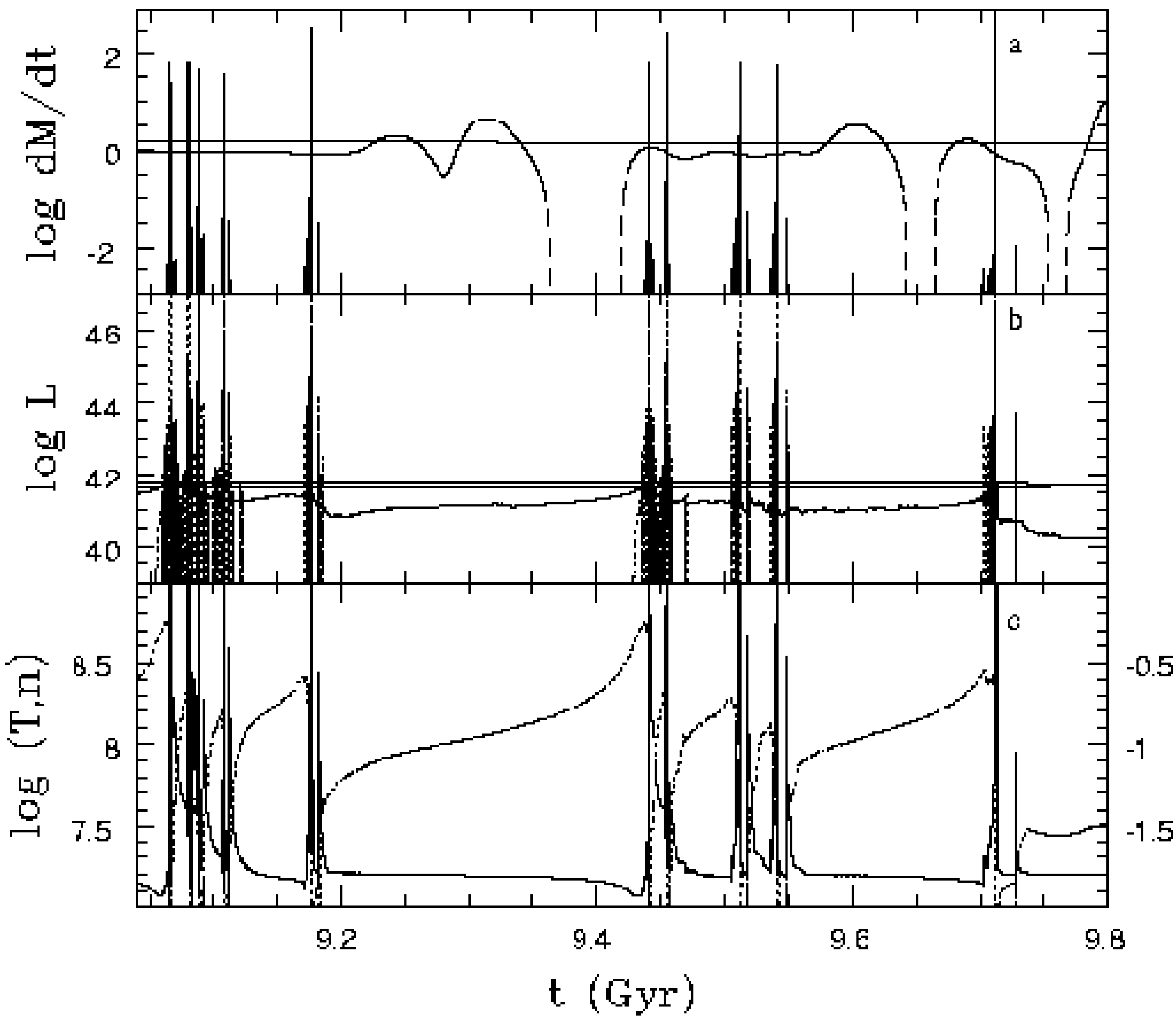

log dM/dt
2
0
-2
a
log L
46
44
42
40
b
log (T,n)
8.5
8
7.5
c
-0.5
-1
-1.5
9.2
9.4
9.6
9.8
t (Gyr)

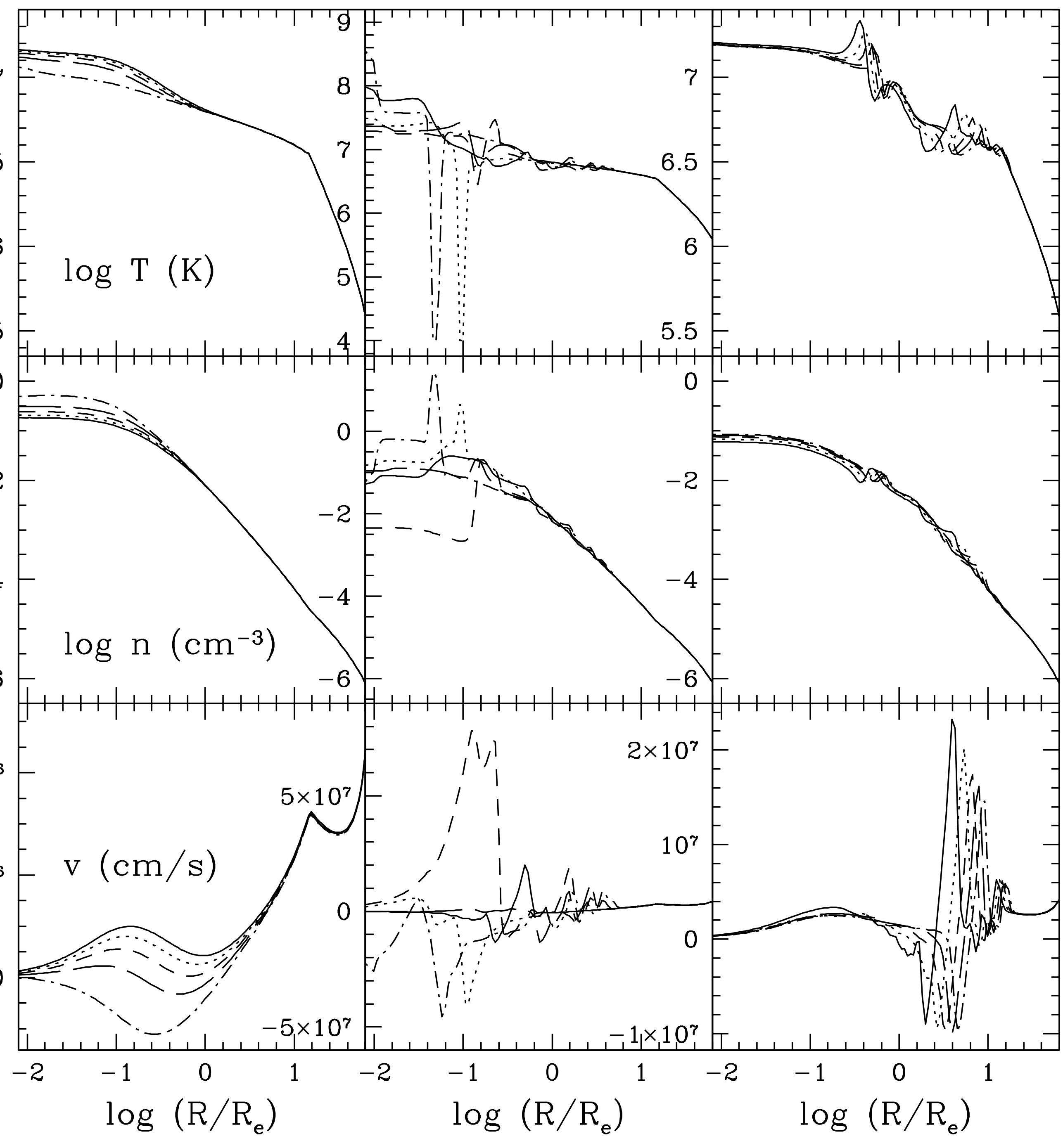

log T (K)
log n (cm^{-3})
v (cm/s)
log (R/R$_e$)
log (R/R$_e$)
log (R/R$_e$)

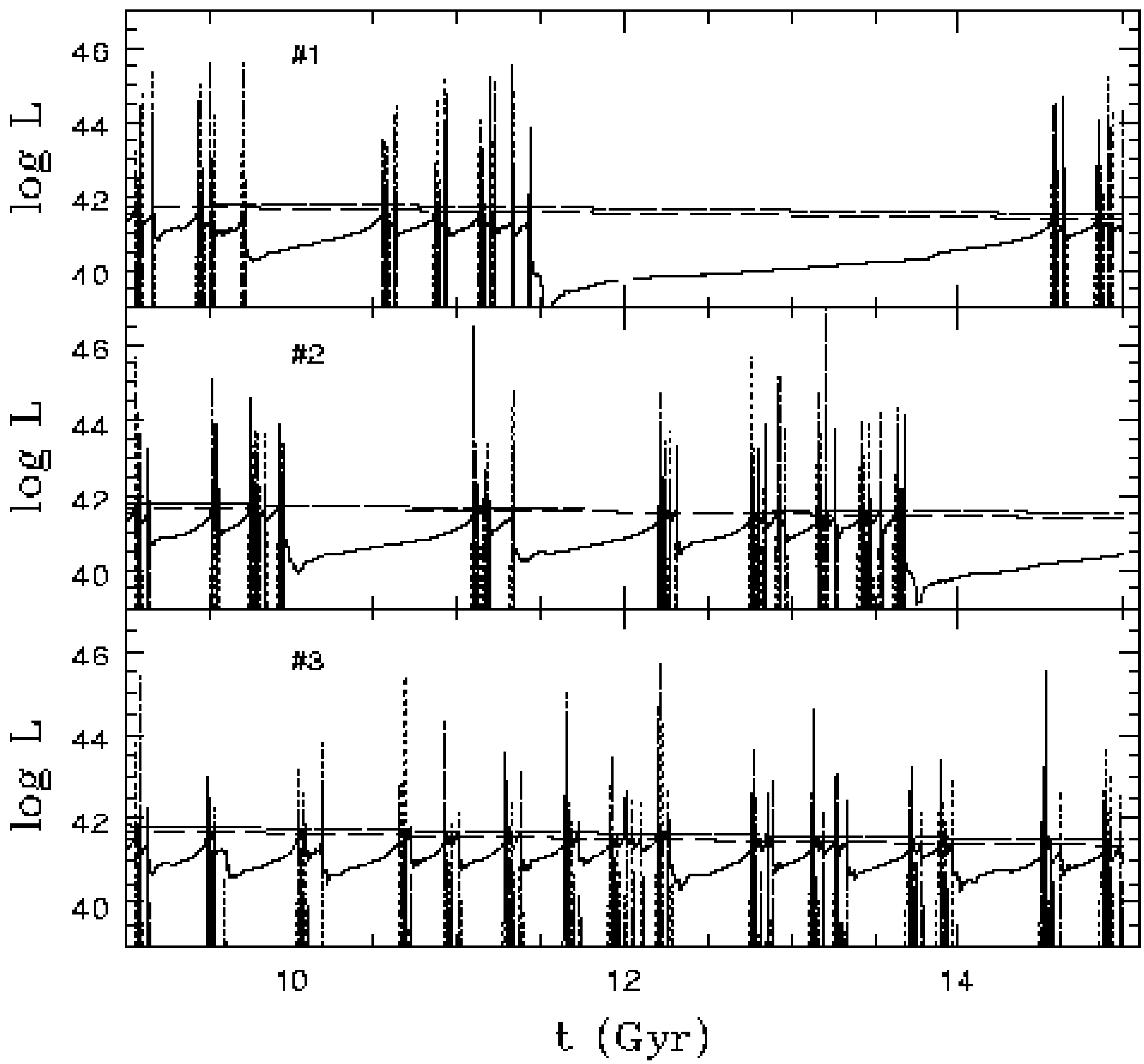

#1
#2
#3
log L
46
44
42
40
10
12
14
t (Gyr)

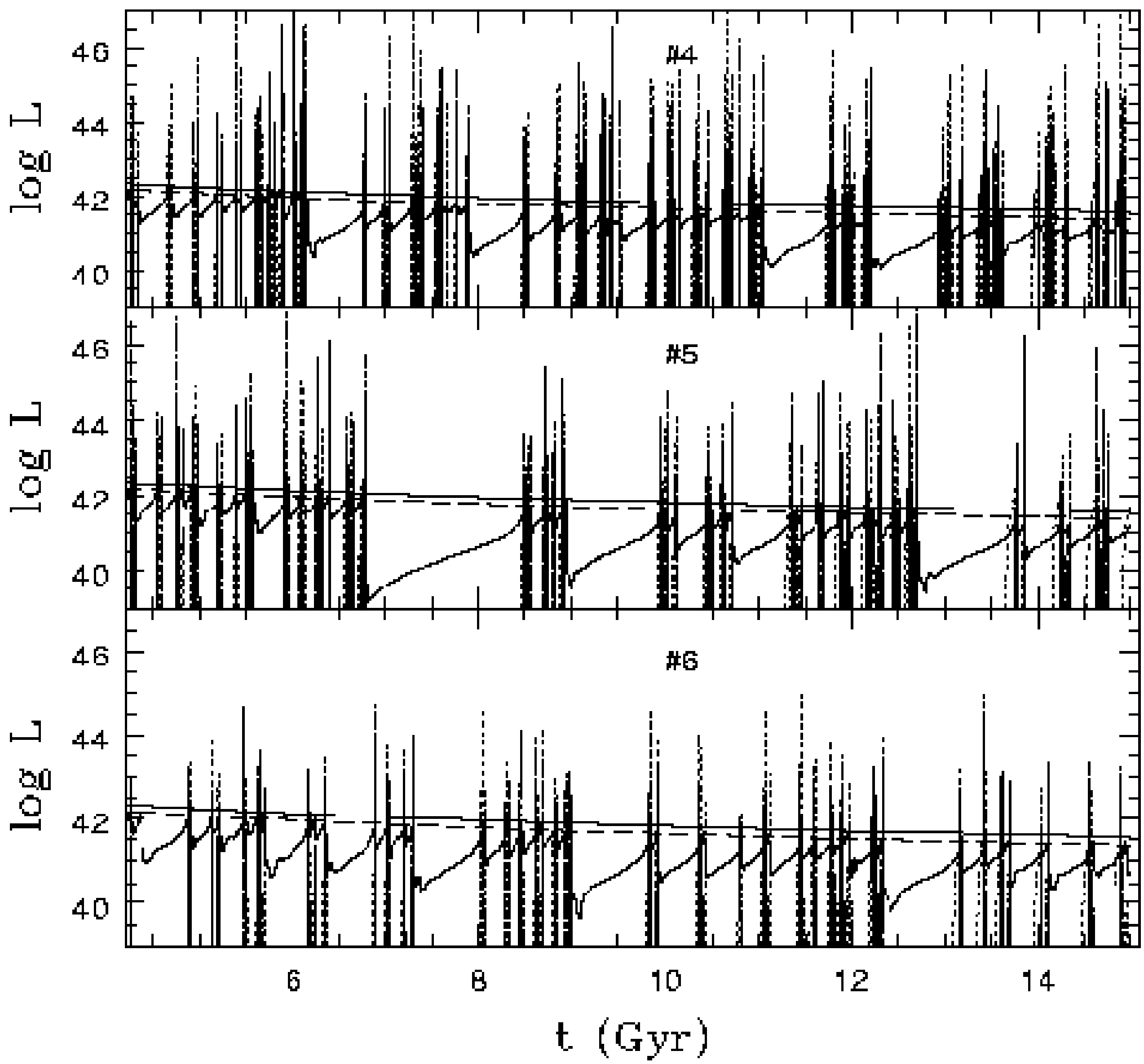
#4
#5
#6
log L
log L
log L
46
44
42
40
6
8
10
12
14
t (Gyr)

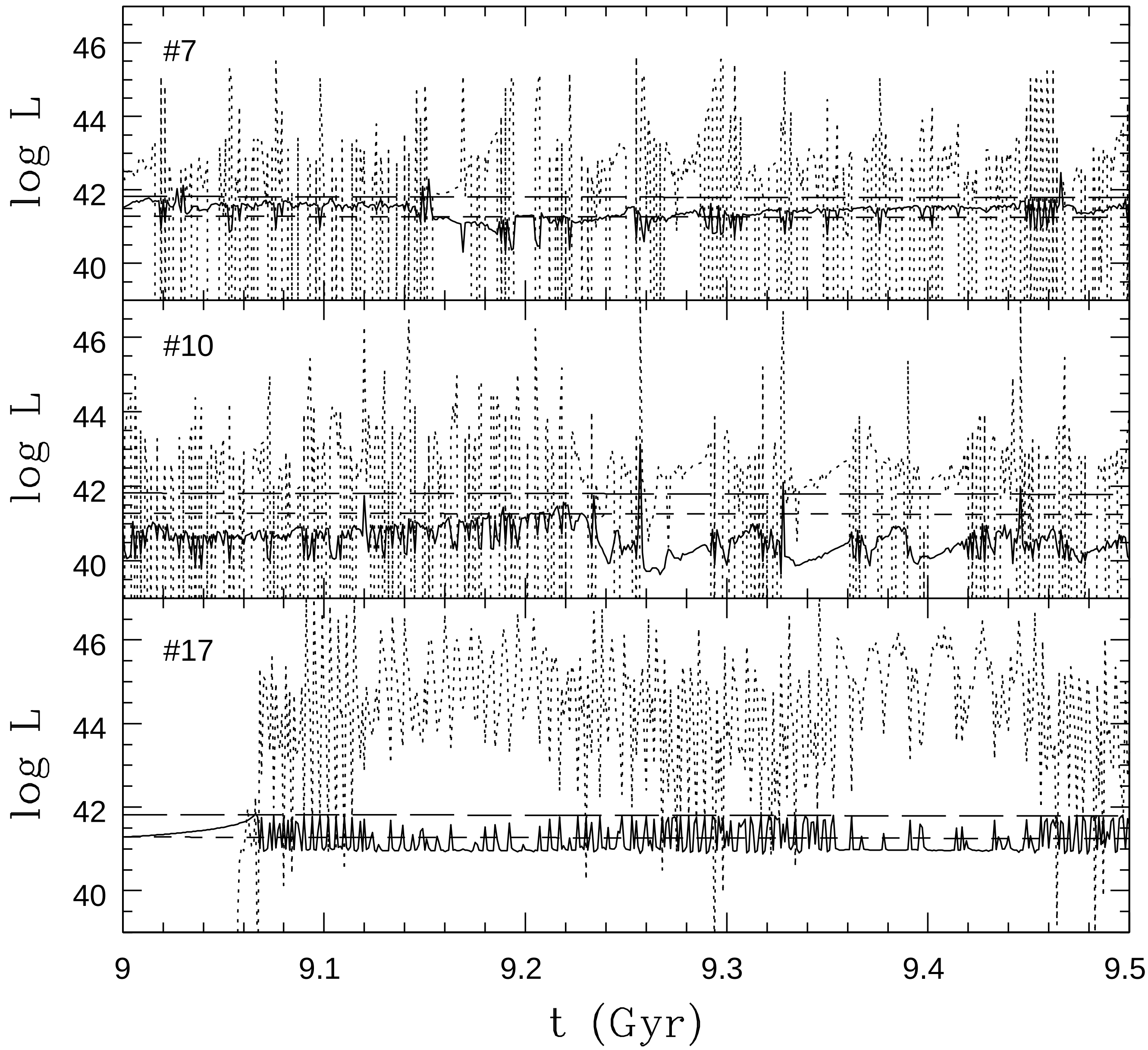

#7
#10
#17
log L
46
44
42
40
9
9.1
9.2
9.3
9.4
9.5
t (Gyr)

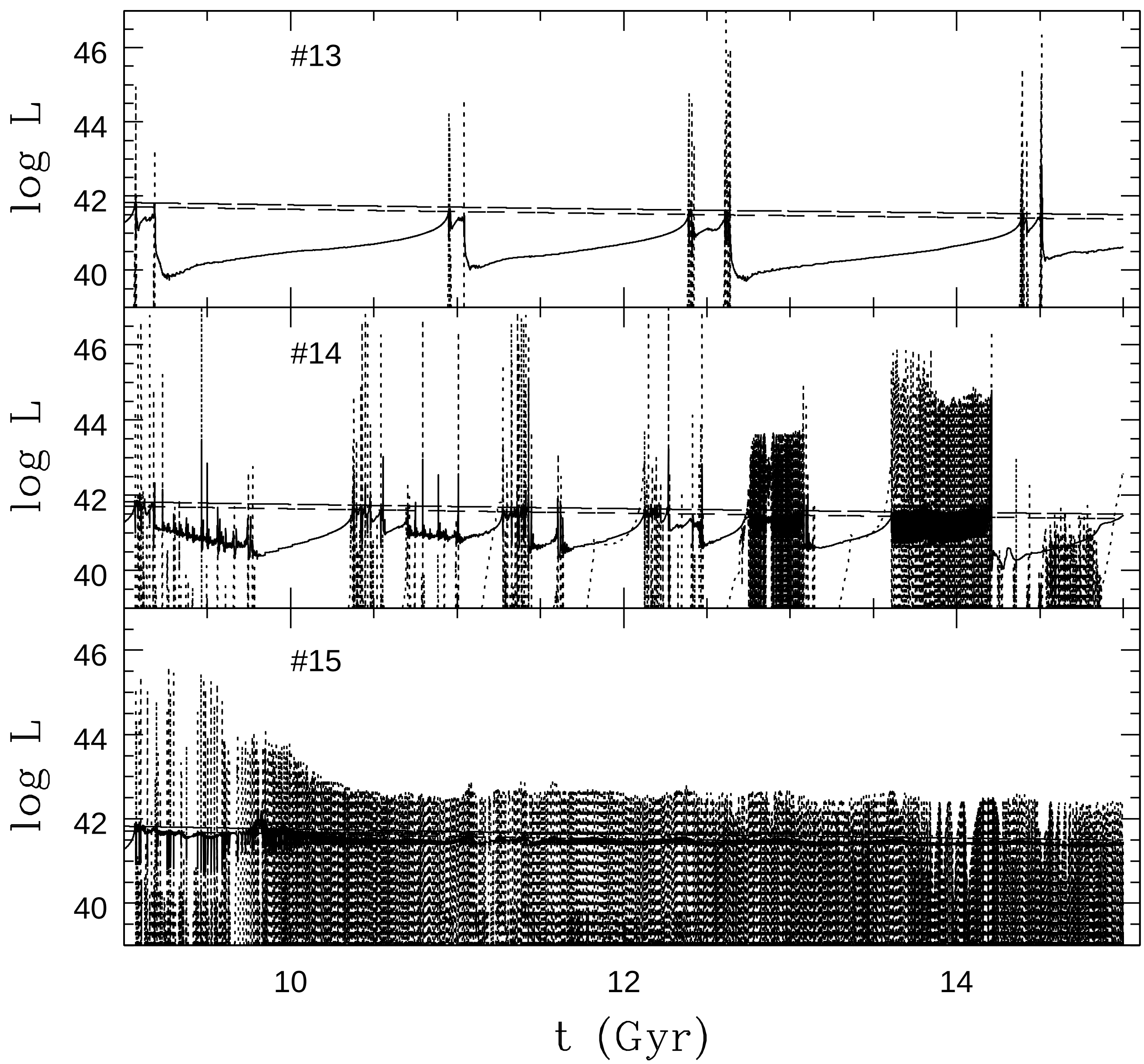
#13
#14
#15
log L
46
44
42
40
10
12
14
t (Gyr)

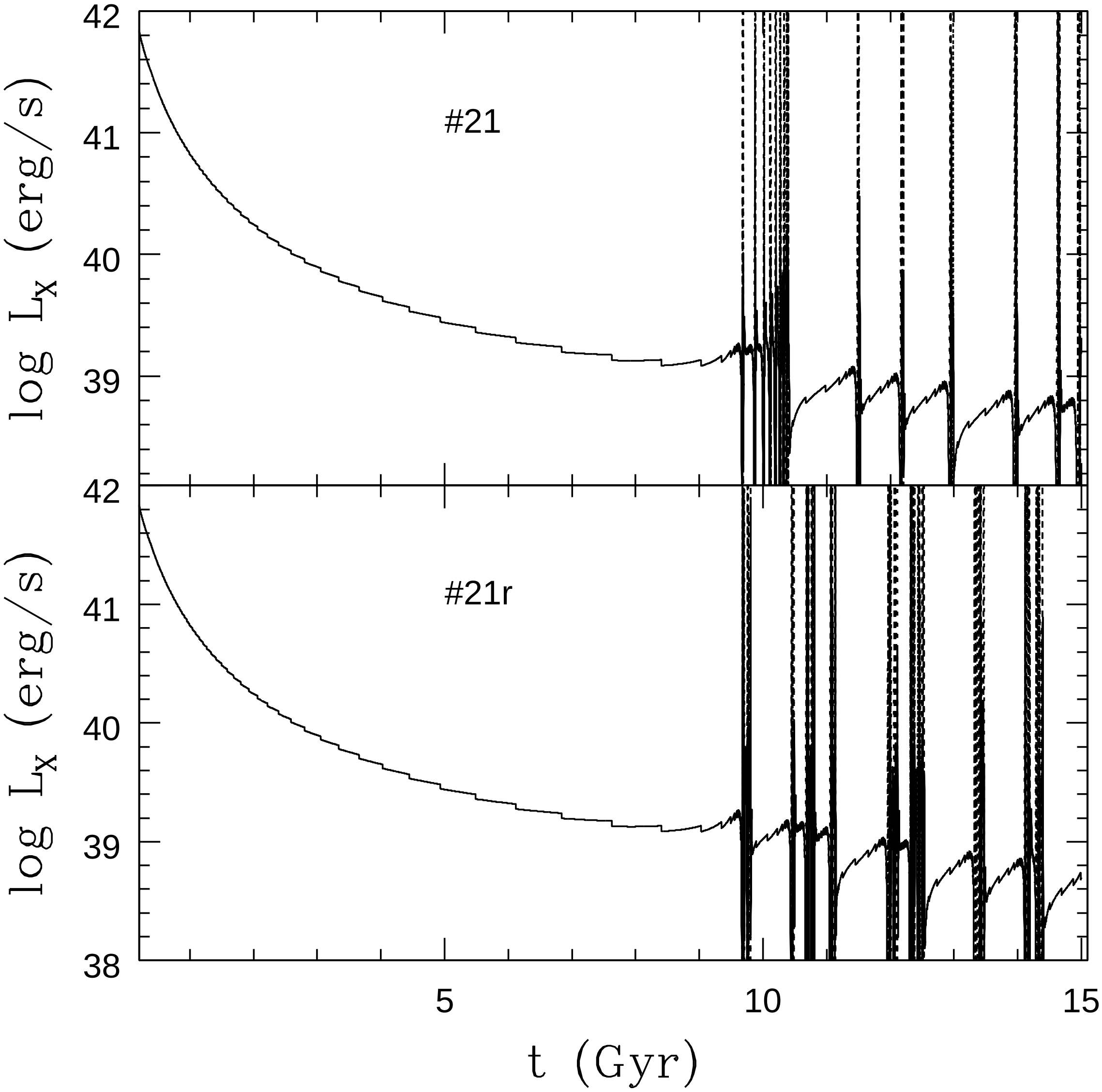
#21
#21r
log L_X (erg/s)
log L_X (erg/s)
42
41
40
39
42
41
40
39
38
5
10
15
t (Gyr)

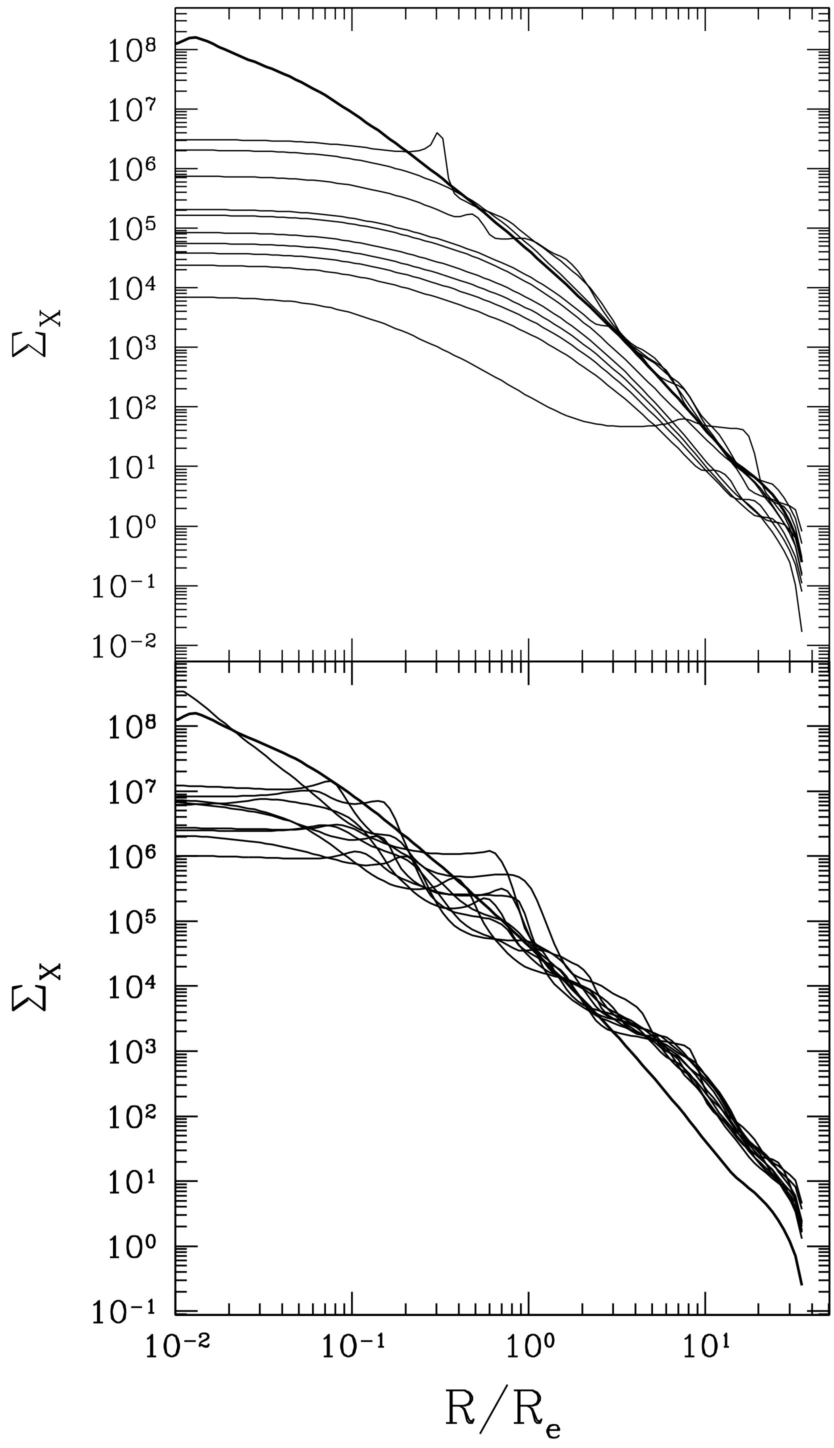
Σ_X
10^{8}
10^{7}
10^{6}
10^{5}
10^{4}
10^{3}
10^{2}
10^{1}
10^{0}
10^{-1}
10^{-2}
Σ_X
10^{8}
10^{7}
10^{6}
10^{5}
10^{4}
10^{3}
10^{2}
10^{1}
10^{0}
10^{-1}
10^{-2}
10^{-1}
10^{0}
10^{1}
R/R_e